Shaping Infrared Light Using Materials with Low and Temperature-Tunable Refractive Indices

by

Alireza Shahsafi

A dissertation submitted in partial fulfillment of the requirements for the degree of
Doctor of Philosophy

(Electrical and Computer Engineering)

at the

University of Wisconsin-Madison
2021

Date of final oral examination: 01/11/2021

The dissertation is approved by the following members of the Final Oral Committee:

Mikhail A. Kats, Associate Professor, Electrical and Computer Engineering

Luke J. Mawst, Professor, Electrical and Computer Engineering

Zongu Yu, Associate Professor, Electrical and Computer Engineering

Jennifer Choy, Assistant Professor, Engineering Physics

In the name of God, the Most Gracious, the Most Merciful

To

My mom and dad,

and to

My lovely late grandfather, Haj Mohsen Bodaghi.

Abstract

This thesis describes several optical demonstrations that enabled new infrared devices, including reflective polarizers, large-area absorbers, and camouflage coatings. For the polarizers and absorbers, my collaborators and I used polar dielectrics materials with unusually low index of refraction in the mid-infrared spectral range. For the camouflage coatings, we used a phase-transition material that undergoes a fully reversible hysteresis-free insulator-to-metal transition.

Acknowledgments

First and foremost, I would like to express my deepest gratitude to my parents, my sister, and my brother-in-law, Dr. Homan Riazi, for the continuous support during my PhD, starting from the application process until now. Second to my family, I'd like to thank my advisor, Professor Mikhail Kats, for his patience, motivation, enthusiasm, and immense knowledge. None of my projects would be possible without his guidance and support. He has guided me since the very beginning and has helped me in conducting my research, attending conferences, and writing my papers. Aside from showing me how to pursue research in a scientific way, Prof. Mikhail Kats has also been a real mentor for me in different aspects of life, from personal and academic growth to becoming an independent researcher. Moreover, he has taught me the importance of building connections and making the best use of every opportunity that comes my way. I could not have imagined having a better advisor and mentor for my PhD. I would also like to also add that he was truly a great friend to me through many difficulties. Also, a very special thanks to my friend, colleague, roommate, officemate and in better words, true brother, Dr. Jad Salman. Thanks for being there for me through hard times, Jad! Furthermore, to my best companion, Dr. Mohammad Ranjbar. Hopefully, we can live next door again someday like PhD times, and complain about different things.

Besides my advisor, I would like to thank the rest of my thesis committee: Prof. Luke Mawst for kindly granting me the opportunity to be his TA, which was an eye-opening experience for me, and for supporting my immigration application. To Professor Jennifer Choy, who has always been supportive and helpful. To Professor Zongfu Yu for the great course of Computational Electromagnetics and the great projects in his group that I was involved in. Thank you all for your encouragement, insightful comments, and constructive feedback on my thesis. Furthermore, I acknowledge the help and support from our collaborators, Professor Shriram Ramanathan and Professor Joanna Aizenberg.

My sincere thanks goes to Majid Shekarchi and all of his family for their immense help and support during the hardest times of the pandemic while I was in a new city far away from my friends and colleagues. Also, many thanks to Majid Aksari, Hossein Panahi and Kaveh Sohrabzadeh and their families. I also want to thank my great friends and their families at UW-Madison, Dr. Amirhossein Davoodi, Dr. Sadegh Mashayekh, Dr. Mohammad Ghaffari, and Dr. Reza Yousefi, and Dr. Ali Kheirandish. I also want to thank my great friends who have showed their continuous support during the ups and downs of these past few years, Saman Cyrus, Yahya Mohtashami, Soroush and Erfan Khorram, Mohammadreza Ranjbr, and Sirous Nourgostar. Also, a special thanks to good friend Haudi Ghiassinejad.

I would like to thank my fellow labmates at UW-Madison at Kats group: Chenghao Wan, Yuzhe Xiao, Jon King, Patrick Roney, Joel Siegel, April Yu, William Derdeyn, Michel Frising, Brad Gundlach, Bryan Rubio, Hongyan Mei, Graham Joe, and Chunhui Yao, for many great collaborations and deep discussions.

Last but not the least, I would like to thank my great team at Quantum-Si, Dr. Faisal Ahmad, and Dr. Michael Bellos who make up the best laser team, along with Dr. Benjamin Cipriany, Dr. Craig Wenger, Patrick Adcock, Andrew Betts, Ali Kabiri, and Ryan Heacox.

Table of Contents

List of Figures

List of Acronyms

n	Real part of refractive index
κ	Imaginary part of refractive index, representative of optical loss
TIR	Total internal reflection
F-TIR	Frustrated total internal reflection
TER	Total external reflection
F-TER	Frustrated total external reflection
FTS	Fourier transfer spectroscopy
TCO	Transparent conductive oxide
SEM	Scanning electron microscope
AAO	Anodic aluminum oxide
SPP	Surface plasmon polariton
SNO/$SmNiO_3$	Samarium nickel oxide
ZDTE	Zero differential thermal emitter
XRD	X-ray power diffraction

List of publications

Leading Author

1. **A. Shahsafi**, J. Salman, B. E. Rubio Perez, Y. Xiao, C. Wan, M. A. Kats. “Infrared polarizer based on direct coupling to surface-plasmon polaritons,” *Nano Letters*, 20(12), p. 8483, 2020.

2. **A. Shahsafi***, P. Roney* (co-lead author), Y. Zhou, Z. Zhang, Y. Xiao, C. Wan, R. Wambold, J. Salman, Z. Yu, J. Li, J. T. Sadowski, R. Comin, S. Ramanathan, M. A. Kats., “Temperature-independent thermal radiation*”, Proceedings of the National Academy of Sciences*, 116(52), p. 2640, 2019.

3. **A. Shahsafi**, G. Joe, S. Brandt, A. V. Shneidman, N. Stanisic, Y. Xiao, R. Wambold, Z. Yu, J. Salman, J. Aizenberg, M. A. Kats. “Wide-angle spectrally selective absorbers and thermal emitters based on inverse opals,” *ACS photonics*, 6(11), p. 2607, 2019.

4. **A. Shahsafi**, Y. Xiao, J. Salman, B. Gundlach, C. Wan, P. Roney, and M. A. Kats, “Mid-infrared optics using dielectrics with refractive indices below unity”, *Physical Review Applied*, 10(3), p. 034019, 2018.

Contributing Author

1. Y. Xiao, C. Wan, **A. Shahsafi**, J. Salman, Z. Yu, R. Wambold, H. Mei & M. A. Kats, Precision Measurements of Temperature-Dependent and Nonequilibrium Thermal Emitters. *Laser & Photonics Reviews*, 14(8), p. 1900443, 2020.

2. Y. Xiao, C. Wan, **A. Shahsafi**, J. Salman, M. A. kats, “Depth Thermography: Noninvasive 3D Temperature Profiling Using Infrared Thermal Emission” *ACS Photonics,* 7 (4), p. 853, 2020.

3. C. Wan, Z. Zhang, D. Woolf, C. M. Hessel, J. Rensberg, J. M. Hensley, Y. Xiao, **A. Shahsafi**, J. Salman, S. Richter, Y. Sun, M. M. Qazilbash, R. Schmidt-Grund, C. Ronning, S. Ramanathan, M. A. Kats, “Optical properties of thin- film vanadium dioxide from the visible to the far infrared”, *Annalen der Physik*, 531 (10), p. 1900188, 2019.

4. Z. Wang, S. Yi, A. Chen, M. Zhou, T. Shan Luk, A. James, J. Nogan, W. Ross, G. Joe, **A. Shahsafi**, K. X. Wang, M. A. Kats and Z. Yu "Single-shot on-chip spectral sensors based on photonic crystal slabs", *Nature Communication*, 10(1020), p. 1, 2019.

5. Y. Xiao, **A. Shahsafi**, C. Wan, P. J Roney, G. Joe, Z. Yu, J. Salman, and M. A Kats "Measuring Thermal Emission Near Room Temperature Using Fourier-Transform Infrared Spectroscopy", *Physical Review Applied*, 11(1), p .014026, 2019.

6. B. S. Gundlach, M. Frising, **A. Shahsafi**, G. Vershbow, C. Wan, J. Salman, B. Rokers, L. Lessard, and M. A. Kats, "Design considerations for the enhancement of human color vision by breaking binocular redundancy", *Scientific Reports*, 8(1), p. 11971, 2018.

7. J. L. King, H. Jo, **A. Shahsafi**, K. Blomstrand, K. Sridharan, and M. A. Kats, "Impact of corrosion on the emissivity of advanced reactor structural alloys", *Journal of Nuclear Materials*, 508(1), p. 465, 2018.

Preprints under review

1. Y. Xiao, C. Wan, J. Salman, I. J. Maywar, J. King, **A. Shahsafi**, M. A. Kats, "Planck spectroscopy", arXiv preprint arXiv:2012.05892, 2020.

2. J. Salman, C. A. Stifler, **A. Shahsafi**, C. Y. Sun, S. Weibel, M. Frising, B.E. Rubio-Perez, Y. Xiao, C. Draves, R.A. Wambold and Z. Yu, "Hyperspectral interference tomography of nacre", arXiv preprint arXiv:2010.08170, 2020, (in revision in PNAS).

3. C. Wan, Z. Zhang, J. Salman, J. King, Y. Xiao, Z. Yu, **A. Shahsafi**, R. Wambold, S. Ramanathan, M. A. Kats, "Broadband reflective optical limiter", arXiv preprint arXiv:2006.03595, 2020.

4. M. Zhou, H. Song, X. Xu, **A. Shahsafi**, Z. Xia, Z. Ma, M. A. Kats, J. Zhu, B. S. Ooi, Q. Gan, Z. Yu, "Accelerating vapor condensation with daytime radiative cooling", arXiv preprint arXiv: 1804.10736, 2018.

Preface

Everything started with an email at the end of November 2014 when I wrote to my current advisor asking if I could be his prospective PhD student. Then, I applied to the University of Wisconsin-Madison, hoping that because of a prior positive communication, I would get admission to join Kats' group. Later, I was lucky enough to be granted school admission on time; however, I did not get my student visa so I was unable to enter the US and start my graduate studies on time. I got my visa a few months later, which was too late to start the semester of Fall 2015. Fortunately, Prof. Kats was kind enough to allow me to start in the Spring of 2016.

While I was in Iran, I received the second important email from Prof. Kats which was about a project that I could start reading and researching about while I was waiting for my move to the United States. That second email shaped my PhD in a great way; it was about the possibility to demonstrate a previously not seen phenomenon called frustrated total external reflection (F-TER), which is similar to frustrated total internal reflection. Although, we were ultimately unable to exactly demonstrate F-TER because *total* reflection requires unrealistically low material losses, I was introduced to the possibility of unusual refractive-index values and their potential for engineering new types of optical devices. Based on this effect, we eventually reported several novel phenomena, and built devices that include a new type of polarizer based on direct coupling of light to surface-plasmon polaritons, published recently in *Nano Letters*.

As I was moving forward with my PhD and working on several research directions made possible using materials with $n < 1$, I also took over the project of one of my great colleagues, Patrick Roney, after he completed his degree. This project was about the engineering of thermal emission using a phase-transition material named samarium nickel oxide. I was very fortunate to work on this project, as I learned a tremendous amount from it. The first major result was published in *PNAS* at the end of last year. After I leave the Kats group, my colleagues will continue to build on this research direction. In this thesis, I will discuss these projects in detail and present many of the results obtained during my graduate studies.

Chapter 1. Introduction

In this chapter, I will briefly talk about the structure of this thesis. In Chapter 2, I report our findings regarding the reflectance of dielectric materials when the real part of their index of refraction is less than one ($n < 1$). Specifically, I present our findings about total external reflection at infrared frequencies, which enables greater reflectance values than those of metallic reference reflectors at oblique incidence angles. Then, I will explain the novel concept of frustrated external reflectance that happens through evanescent wave coupling.

In Chapter 3, I show our results about coupling light into surface waves that propagate at a dielectric–metal interface without using any surface modulations. Our approach is similar to the “Kretschmann” and “Otto” configurations that are well-known in the plasmonics field, but unlike these two configurations our approach uses no prisms. Instead, the coupling is enabled by the decrease of the surface-plasmon wavevector for $n < 1$ dielectric materials compared to more-conventional materials with $n > 1$.

In Chapter 4, I discuss our collaborative results with Harvard and Purdue, on engineering of thermal emission. In the first section of this chapter, I describe our spectrally selective absorber/emitter based on inverse-opal-type metamaterials synthesized at Harvard University in the Aizenberg group. Our metamaterial device shows excellent thermal stability, and high absorption for a broad angular range for both polarizations. In the second section, I show our results on temperature-independent thermal emission using samarium nickel oxide, a novel phase-transition material, grown at in the Ramanathan group at

Purdue University. The demonstrated thermal emitter can be used for passive and fully reversible infrared camouflage and thermal regulation applications.

At the end of this document, there are a few appendices that describe how we conducted some modeling/simulation and measurements as well as more detailed discussions about measurement of refractive index of SiO_2 and the metal-to-insulator transition of $SmNiO_3$.

Chapter 2. Reflective behavior of dielectrics with $n < 1$

Motivation

My journey into dielectric materials with refractive index, n, less than one ($n < 1$), started with thinking about possible demonstration of a previously not demonstrated optical effect named frustrated total external reflection (F-TER)—an analog of frustrated total internal reflection but with light incident from air rather than from within a high-index material. Basically, we were looking to do experiments using a low-loss material in which the real part of its refractive index, n, is less than one. With light shining on such a material at oblique angles (while the incident angle is greater than critical angle and there is an evanescent wave inside the second layer), we wanted to show that light can get coupled to a third medium through evanescent-wave coupling. This may happen when the thickness of the material with $n < 1$ is in order of penetration depth of evanescent wave. We first started looking at conductive oxides or so-called transparent conductive oxides (TCOs). As I show in the last figure of this chapter, the optical loss of TCOs is much larger than that of polar-dielectric materials in the mid-infrared range due to nature of resonances behind the decrease of refractive index in polar-dielectric materials. Thus, we chose to work with polar dielectrics materials such as SiO_2 and Al_2O_3.

As we were trying to demonstrate F-TER, we also explored other interesting phenomena that can happen when the refractive index of a material is less than the refractive index of air. This chapter and next one is mainly focused on these novel optical phenomena. Note that the material in this chapter has been published as Shahsafi, Alireza, et al. "Mid-infrared optics using dielectrics with refractive indices below unity." *Physical Review Applied* 10.3 (2018): 034019.

1. Introduction

In traditional optical elements such as lenses, materials are used in the spectral regions that they are totally transparent, and typically have refractive indices (n) between 1 and 4 [1]. In such regions, these materials are devoid of optical resonances, resulting in negligible optical losses. Recently, the use of both intrinsic and engineered resonances has enabled the demonstration of a number of exotic optical phenomena, especially in the field of metamaterials [2]. For example, resonances in both the permittivity, ϵ, and permeability, μ, can result in a negative index of refraction ($n = \sqrt{\epsilon\mu} < 0$) [3]–[5]. Similarly, by using electric or magnetic resonances, the values of ϵ or μ can be made to approach zero (*i.e.*, “epsilon-near-zero”, or “mu-near-zero”, respectively), resulting in a near-zero refractive index ($n \sim 0$) [6], [7]. In such a material, light can propagate without accumulating phase, enabling unique phenomena such as super-coupling [8]. Furthermore, by using materials that have $n < 1$, it is shown that invisibiliy cloaking can be achieved, because only in this case light may go around the object without causing phase distortion [9]. Unfortunately, in many instances, the promise of these exotic phenomena and applications is tempered by optical losses, which are enhanced in close proximity to resonances [10], [11].

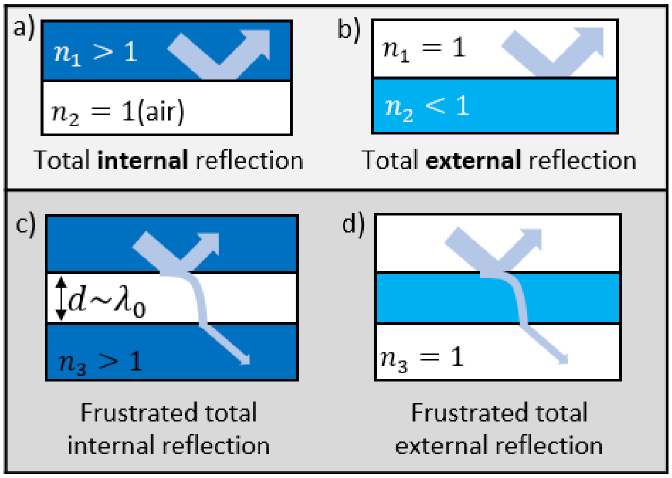

Figure 2-1) Two well-known optical phenomena (left), and their less-conventional counterparts enabled by materials with n < 1 (right).**(a)** Total reflection for light incident from a high-index region (1) to air (2), and **(b)** from air (1) to a low-index region (2). **(c-d)** If the thickness of region 2 is comparable to the wavelength of light, λ_0, and a higher-index region 3 is introduced below, some light can be transmitted. This is referred to as frustrated total internal reflection if $n_1 > 1$; by analogy, we refer to the case when $n_1 = 1$ as frustrated total external reflection

In this section, we explore optical phenomena within a spectral range that is close — but not too close — to strong optically active resonances, resulting in the reduction of the real part of the refractive index to below that of vacuum (*i.e.*, $0 < n < 1$). Our demonstrations use a simple homogeneous material, fused silica (SiO_2), which has strong optical-phonon resonances in the mid infrared [12], but is transparent in the visible and near infrared. The intermediate proximity to these optical-phonon resonances results in only a modest increase in the losses, quantified by a small imaginary part of the refractive index, κ. By utilizing the reduction of refractive index in SiO_2 to below one in a portion of the long-wave infrared region, we experimentally demonstrate two unusual optical phenomena in this chapter, including external reflection [(Fig. 2(2-1b)] and its frustration [(Fig. (2-1d)].

2. Optical properties of SiO_2

Optical-phonon resonances of dielectric materials such as SiO_2 or aluminum oxide (Al_2O_3) typically lie in the mid-infrared spectral range The resulting optical properties can be described by Lorentz [13], Gaussian [14], or similar oscillator models and, in the vicinity of such resonances, the refractive index can be below unity [12].

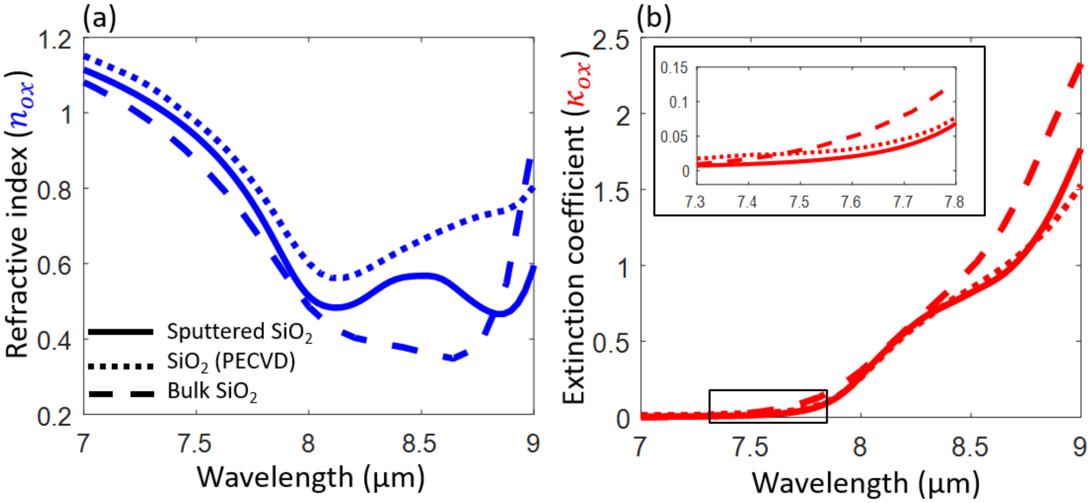

Figure 2-2) Optical properties of SiO_2.

(a) Real (n_{ox}) and **(b)** imaginary (κ_{ox}) parts of the complex refractive index of fused silica (SiO_2) close to its phonon resonances. Two sets of experimentally obtained refractive indices are presented: one of a film grown via plasma-enhanced chemical vapor deposition (PECVD, dotted), and the other from an SiO_2 wafer. For comparison, data taken from ref. [12] are shown using solid lines. Inset: zoomed-in plot of κ_{ox} in a region where $n_{\mathrm{ox}} < 1$ and the losses are relatively small.

We used two types of SiO_2 for the various experiments: thin films grown via plasma-enhanced chemical vapor deposition (PECVD) on high-resistivity silicon, and bulk SiO_2 wafers. The measured refractive index, n_{ox}, and extinction coefficient, κ_{ox}, of these are shown in the Fig. 2-2 [12], [14]–[16], and compared to literature data [12]. Though the optical properties differ somewhat between the different samples, in all cases κ_{ox} is relatively small as n_{ox} approaches 1. Specifically, in the 7.3 ~ 7.7 μm region, $n_{\mathrm{ox}} < 1$ and $\kappa_{\mathrm{ox}} < 0.05$. In ideal case of negligible optical loss, the transition to total reflection for example is fast. To show this in a clear way, we conducted thin-film calculations in which light is shining at a material with refractive index of $\tilde{n} = n + i\kappa$. In Fig. 2-3 (a, b), it is assumed that n is constant and smaller than one (in this case, 0.7), and κ varies. These plots show that a sharper/faster transition to external reflection can be achieved by using a material with lower loss.

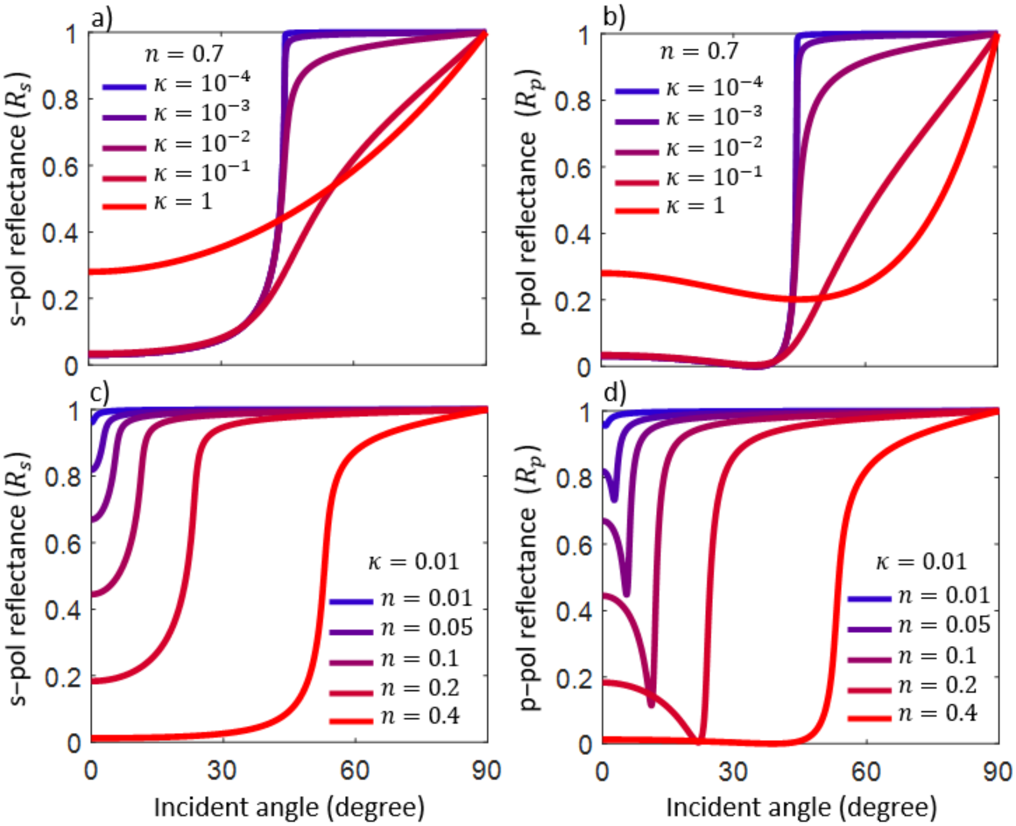

Figure 2-3) Transition to total external reflection with various values of n and κ

(a,b) The increase of optical loss (κ) smooths the transition to total reflection. (c, d) Change of refractive index (n) changes the critical angle.

Setting a constant κ for the material with $n < 1$ and sweeping n results in different critical angles of external reflection [Fig. 2-3(c, d)]. Also, increasing n results in a more gradual transition. To consider the effect of both n and κ, we used a figure of merit, $\eta = \kappa/(1 - n)$, used at X-ray frequencies [17]. A decrease of η results in a sharper transition to total external reflection. In Fig. 2-4, we plot the polarization-averaged reflection of several materials with $n < 1$, versus the incident angle divided by the critical angle, at the wavelengths at which η is minimum.

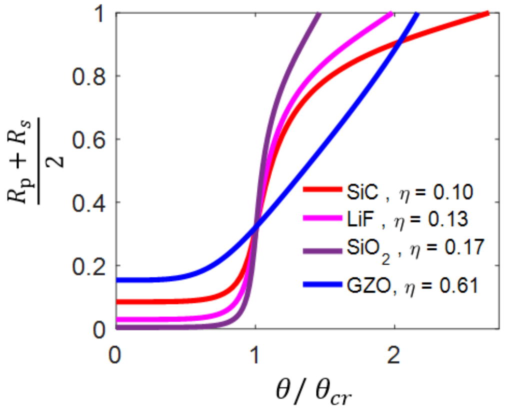

Figure 2-4) Polarization-averaged reflectance versus incident angle

This data is normalized to the critical angle, for several representative materials with n<1. Each plot is at the wavelength for which η is minimum for that material.

3. Results and discussion

a. Greater reflection than noble metals

When light is incident on a low-index (n_2) material from a high-index (n_1) material, total internal reflection (TIR) occurs for incident angles greater than the critical angle ($\theta_{cr} = \arcsin(n_2/n_1)$) [Fig. (2-1a)]. In TIR, the incident medium is usually an optically dense material such as glass. Analogously, when the incident medium is air, and the second material has $n < 1$, a similar phenomenon occurs, referred to as total external reflection (TER) [Fig. (2-1a)]. TER is well-known at X-ray frequencies, where complex refractive indices are often written in the form: $\tilde{n} = 1 - \Delta + i\beta$, where typically $\Delta \sim 10^{-5}$ and $\beta \sim 10^{-7}$ [18]. Mirrors based on TER are used for X-ray focusing and other applications [19], [20], and air-core waveguides using TER have been explored theoretically [21].

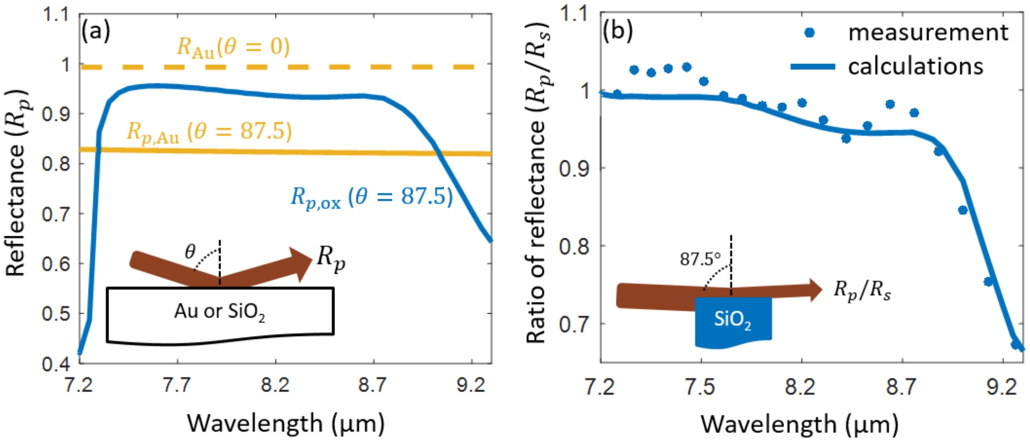

Figure 2-5) Oblique-angle reflection of SiO$_2$ can surpass that of gold.

(a) Transmittance and **(b)** reflectance of an SiO$_2$ film on a silicon substrate, for p-polarized light versus incident angle at $\lambda_0 = 7.8$ µm, for three different film thicknesses of SiO$_2$, d. The $d = 6$ µm film is significantly thicker than the evanescent decay length δ, so almost no light is transmitted for incident angles beyond θ_{cr}, maximizing reflectance. Conversely, for the thinner films, the transmittance does not drop completely to zero, and the reflectance is reduced, indicating frustrated external reflection (F-ER). θ_{cr} is identified with a vertical dashed grey line.

In the mid infrared, metallic mirrors can have reflectances of ~ 99% [22], and are often used as references for reflectance measurements. However, for very oblique incidence angles and p polarization, even gold and silver mirrors have a reduced reflectance due to the pseudo-Brewster effect [23], [24]. Polished gold mirrors, for example, have significantly decreased reflectance at angles of incidence between 80° and 89° in the near to mid infrared [*e.g.*, Fig. (2-5 a)]. By comparison, due to TER, materials with $n < 1$ can be used to achieve much larger p-polarized reflectance for these highly oblique angles. We calculated and measured the p-polarized reflectance of an SiO$_2$ wafer at an incident angle of 87.5° Fig. 2-5, and found reflectance values of ~ 95%, compared to ~ 82% for gold for λ_0 =7.3 ~ 8.7 μm; the SiO$_2$ p-polarized reflectance is higher than that of gold for angles > 85° [15], [24]–[26]. We note that due to the highly oblique angle of incidence and relatively small sample area, we were not able to accurately measure the absolute reflectance, because the beam cross section was larger than our sample (see Fig. 2-5 (b) inset). Instead, we measured the ratio of p-polarized and s-polarized reflectance, eliminating the need for a reference [Fig. 2-5 (b)]. This figure shows good agreement between the measurement and calculations based on Fresnel equations, using the refractive index data in Fig. 2-2.

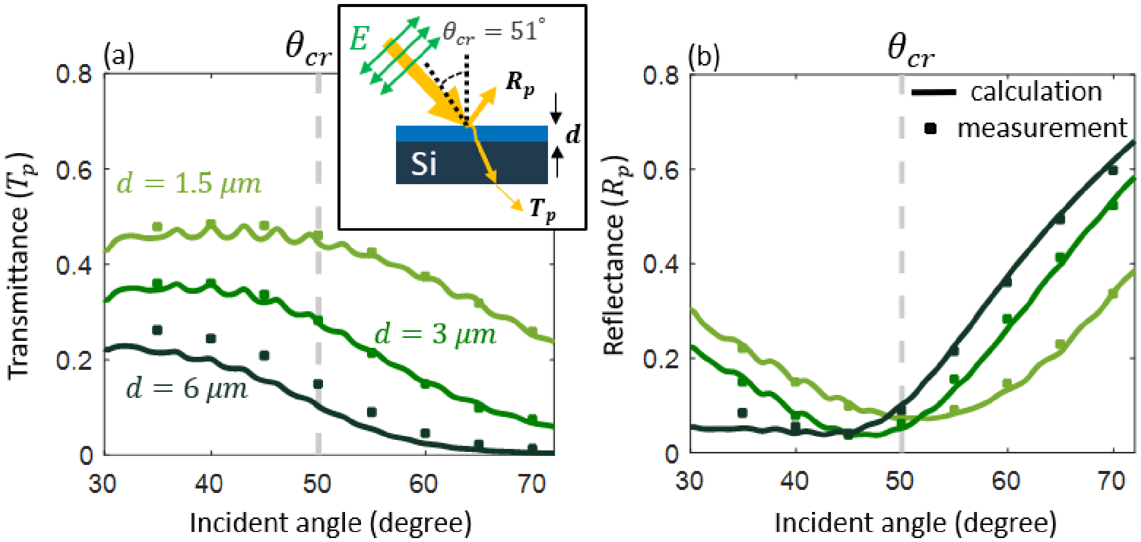

Figure 2-6) Frustration of external reflection.

(a) Transmittance and **(b)** reflectance of an SiO_2 film on a silicon substrate, for p-polarized light versus incident angle at $\lambda_0 = 7.8\ \mu m$, for three different film thicknesses of SiO_2, d. The $d = 6\ \mu m$ film is significantly thicker than the evanescent decay length δ, so almost no light is transmitted for incident angles beyond θ_{cr}, maximizing reflectance. Conversely, for the thinner films, the transmittance does not drop completely to zero, and the reflectance is reduced, indicating frustrated external reflection (F-ER). θ_{cr} is identified with a vertical dashed grey line.

b. Frustrated *total* external reflection

In both TIR and TER, light is incident on a material with a lower refractive index from a material with higher refractive index, at an angle greater than the critical angle, θ_{cr} (Fig. 2-1 (a-b)). In both cases, the electric field just beyond the interface does not abruptly drop to zero, but decays exponentially as an evanescent wave [25]. When the lower-index material has a thickness on the order of the evanescent-wave decay length, light can tunnel through the material and emerge on the other side. This is referred to as frustrated total internal reflection (F-TIR) [27] [28] [Fig. 2-1 (c)], and has numerous applications such as multi-touch sensing [27]. Analogously, this process can take place for external reflection, which we refer to as *frustrated external reflection* (F-ER; here we omit 'total' from the term due to the non-zero optical losses).

c. Frustrated external reflection

We calculated the decay length of the evanescent wave [29] to approximately obtain the SiO_2 film thickness required for observation of F-ER [29]. To demonstrate F-ER experimentally, we deposited three SiO_2 films with thicknesses of 1.5, 3, and 6 μm onto double-side-polished high-resistivity silicon wafers using PECVD. At $\lambda_0 = 7.8\,\mu m$, these films have $\tilde{n}_{\mathrm{ox}} = 0.8 + 0.07i$ (Fig. 2-2), and thus $\theta_{cr} = 51°$. In Fig. 2-6 (a), we show the measured and calculated transmittance versus the incident angle for p polarization. The calculations were performed using the transfer matrix method [15], assuming a silicon substrate thickness of 500 μm. The fine fringes in the calculated data, which are due to thin-film interference in the silicon, are not observed in the experiment most likely because of the non-zero numerical aperture (*i.e.*, each measurement corresponds to an average over a range of incident angles). The plotted calculated data was smoothed using a moving average to roughly emulate the measurement. Figure 2-6 (a) shows that some light is transmitted even for $\theta > \theta_{\mathrm{cr}}$, demonstrating F-ER. As expected, an increase of the thickness of the SiO_2 layer (d) results in lower transmittance.

For $\theta > \theta_{\mathrm{cr}}$, the reflectance increases with increasing d (Fig. 2-6 (b)), as the effect of frustration is reduced. For $\theta < \theta_{\mathrm{cr}}$, however, increasing d results in a decrease in reflectance. This occurs because $|\tilde{n}_{\mathrm{ox}}|$ is close to 1 (*i.e.*, the refractive index of air), so most of the reflected light comes from the SiO_2/Si interface rather than the air/SiO_2 interface. A thicker SiO_2 film absorbs more light, reducing the overall intensity that emerges back into the air. At angles beyond θ_{cr}, the slope of the transmittance vs. angle changes, indicating the onset of F-ER [see Fig. (2-6 a)]. Note that the reflectance does not reach unity even at very oblique angles because of evanescent-wave absorption within the SiO_2 (*i.e.*, no *total* external reflection).

d. Frustrated *total* external reflection calculation

Figure (2-7) shows the calculation of reflection and transmission versus incident angle for the same structure of SiO_2 on top of silicon substrate, assuming there is no optical loss in the SiO_2 ($\kappa_{\mathrm{ox}} = 0$), but the same n_{ox} as SiO_2 has in Fig. 2-2 (a). This calculation was done to analyze frustrated *total* external reflection, and it shows that the transition to total reflection occurs much faster across the critical angle compared to the real case with optical loss. Similarly, to the real case with losses, the transition happens more gradually for thinner films. Note that there exists an angle in both the angular reflection and transmission plots at which the curves for different thickness overlap; this corresponds to the Brewster angle at the SiO_2/Si interface. At this angle, the reflection from the structure is dominated by the air/SiO_2 interface; therefore, reflection becomes independent of the film thickness.

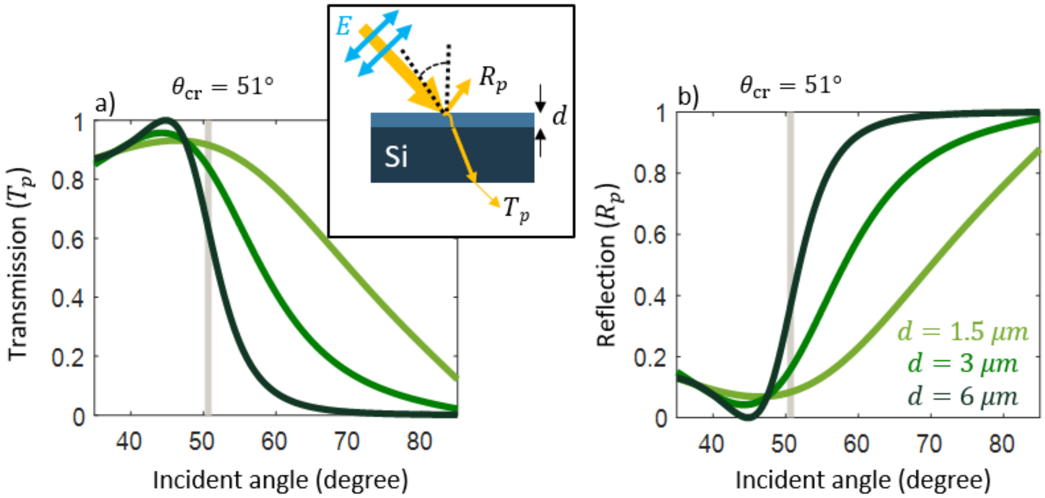

Figure 2-7) Frustrated total external reflection

(a) Transmittance and (b) reflectance of a fictitious SiO_2 film without optical loss on a silicon substrate, for p-polarized light, versus incident angle at $\lambda_0 = 7.8\ \mu m$, for three different film thicknesses of SiO_2, *d*. θ_{cr} is identified with a vertical grey line.

4. Other materials

The phenomena described in this paper all become easier to observe for materials that simultaneously have n significantly below 1 and minimal losses. However, the frequency dependences of n and κ are always connected (as described by the Kramers-Kronig relations [30]) and generally have an inverse relationship; *e.g.*, the reduction of n in SiO_2 is accompanied by an increase of κ on the lower-loss side of the resonance (Fig. 2-2). To evaluate candidate materials, we define a figure of merit that simultaneously quantifies the loss and the difference of n from unity: $\eta = \kappa/(1-n)$. This figure of merit is used in the X-ray regime to quantify the sharpness of the transition between ordinary and external reflection [17]. In Fig. 2-8, we plotted η as a function of frequency in the near and mid infrared for several candidate materials with optical-phonon or plasma resonances [12], [31]. Among the materials we explored, silicon carbide reaches the smallest value of η

[32], and lithium fluoride has the longest wavelength span for which $n < 1$ and $\eta < 1$ [33]. In general, fluorides seem to be good candidate materials [34], with the wavelength of the $n < 1$ region increasing for larger cations. We note that many of these candidate materials are transparent with $n > 1$ at shorter wavelengths (*e.g.*, in the visible), potentially enabling very different functionalities in different spectral ranges.

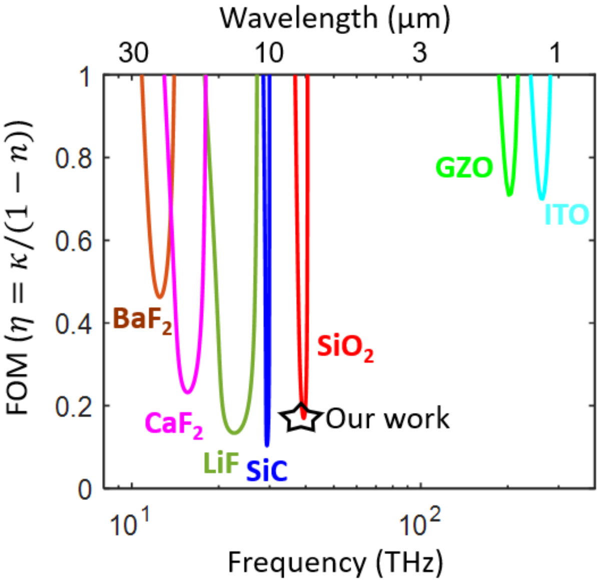

Figure 2-8) Figure of merit, η = κ/(1-n), for several candidate materials with n < 1.

This figure included transparent conducting oxides in the near infrared and dielectric materials with strong phonon resonances in the mid infrared (material data from refs. [12], [34], [35], [36], and [37].)

In conclusion, we explored the use of low-loss materials with refractive index below unity ($n < 1$) to “invert” several well-known configurations in optics that are based on total or attenuated internal reflection. We showed that transparent dielectrics in visible range, with strong phonon resonances at mid-infrared frequencies are good candidate materials for such applications, experimentally demonstrating *external reflection*, *frustrated external reflection*, and *direct coupling to surface plasmon polaritons* from free space without using prisms or surface modulation. We envision potential applications of the $n < 1$ region in these dielectrics and other materials with low-loss resonances for spectral or angular filtering, air-core waveguiding, and surface-plasmon-based sensing.

Chapter 3. Directly coupling to surface plasmon polaritons

Motivation

In this chapter, I describe a new mechanism of coupling to surface plasmon polaritons (SPPs). Fig. 3-1 shows our approaches in two different ways which are similar to Kretschmann [35] and Otto configurations [36], which are coupling methods that use prisms to enhance the wave vector of incident light and thus enable coupling to bound SPPs. This leads us to a second approach, similar to the Otto configuration, and we demonstrated very efficient coupling by using anodic aluminum oxide as a material with $n < 1$.

As there is no bulky prism on top of the structure to match wavevector of incident light to that of the SPP in this way of coupling, we used the concept to demonstrate a new type of reflective polarizer that has a high extinction ratio and high efficiency at infrared frequencies. The material in this chapter has been published as A. Shahsafi, et al. "Mid-infrared optics using dielectrics with refractive indices below unity." *Physical Review Applied* 10.3 (2018): 034019, and A. Shahsafi, et al. "Infrared Polarizer Based on Direct Coupling to Surface Plasmon Polaritons." *Nano Letters* 20.12 (2020): 8483.

1. **Introduction**

SPPs are surface waves that propagate at the interface between a metal and a dielectric [37]. To excite SPPs from free space, incident light with a certain frequency and wave vector (projected onto the direction of the interface) are required. Usually, the wave vector of the incident light has a smaller value than the SPP wave vector at the same frequency, making coupling difficult. A standard approach to enable coupling uses prisms comprising high-index dielectric materials to increase the wave vector of the incident light to match with that of the SPP—in particular, in the Kretschmann [35] [Fig. 1(a)] and Otto [36] [Fig. 1(b)] configurations. In the Kretschmann configuration, light inside the prism reaches a thin metal layer and tunnels through to the SPP mode on the other side [Fig. 1(a)]. In the Otto configuration, light tunnels through a small dielectric gap before reaching the SPP mode [Fig. 1(b)]. Note that, in either case, SPPs can only be excited by light polarized parallel to the plane of incidence (p polarization), whereas light in the other polarization is mostly reflected [37]. In this chapter, first, we show how we couple light in similar structure to the Kretschmann configuration [Fig. 3-1(c)] [35], and then we present our results for the Otto configuration [Fig. 3-1(d)] [36]. Both modified coupling techniques are enabled because we can decrease the wavevector of SPPs by using a $n < 1$ material. We note that coupling to such a leaky SPP mode is sometimes referred to as the Berreman effect [38]–[40], though we find the connection to the well-known Otto and Kretschmann configurations for SPP coupling to be more instructive and thus prefer that language.

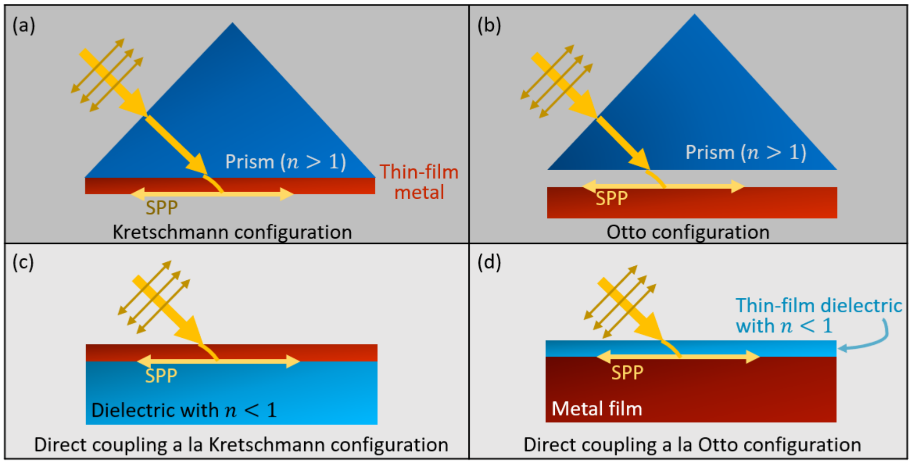

Figure 3-1) Surface plasmon polaritons excitations

(a, b) Excitation of SPPs using a prism in the (a) Kretschmann configuration [35] and (b) Otto configuration [36]. **(c, d)** Prism-free direct coupling to SPPs in the modified (a) Kretschmann and (b) Otto configurations by using a dielectric with real part of its refractive index less than one, resulting in a decrease of the SPP wavevector [41].

2. Kretschmann configuration

As we described in the previous chapter, the use of materials with $n < 1$ allows us to "invert" many common configurations in optics, using air as a high-index medium (Fig. 2-1). In this chapter, we explored replacing the high-index prism in the well-known Kretschmann configuration for coupling to surface-plasmon polaritons (SPPs) [35] with air. Specifically, we explore coupling to SPPs at the interface between gold (Au) and SiO_2, in the 7.4 – 7.7 μm wavelength region, where $n_{\mathrm{ox}} < 1$ and $\kappa_{\mathrm{ox}} < 0.08$ (Fig. 2-2).

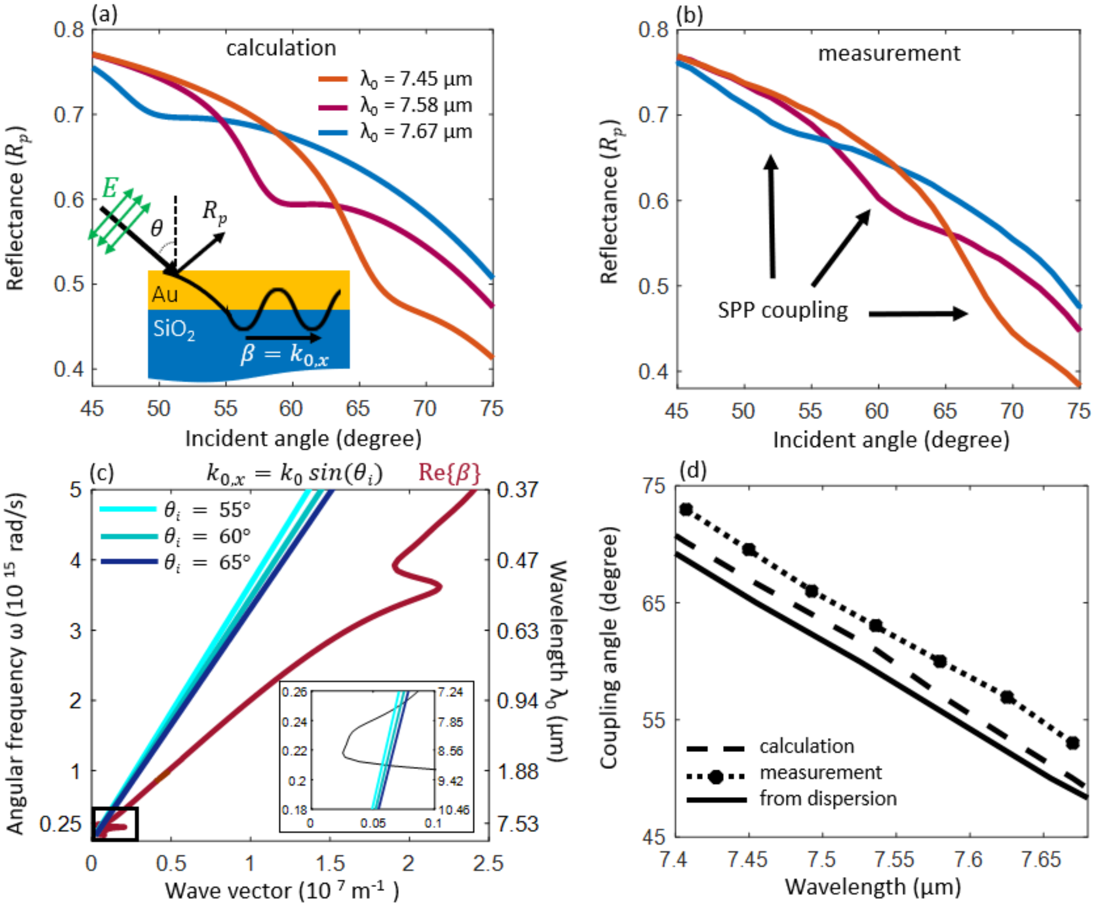

Figure 3-2) Direct coupling to SPPs from free space

(a) Calculated and **(b)** measured p-polarized angle-dependent reflectance of a 10 nm Au film deposited on an SiO_2 substrate at $\lambda_0 = 7.45, 7.58,$ and $7.67\ \mu\mathrm{m}$, corresponding to $n_{\mathrm{ox}} = 0.9, 0.84,$ and 0.76, respectively. The dips are evidence of coupling to SPPs at the interface between Au and SiO_2. **(c)** Dispersion plots for incident light for different angles, and SPPs at the Au/SiO_2 interface. The intersections around 7.5 μm (see inset) correspond to locations of the dips in the reflectance curves in (a, b). Three blue traces show $k_{0,x}$, the x-component of the wave vector of the incident light for $\theta_i = 55, 60, 65°$. Smaller angles of incidence correspond to smaller $k_{0,x}$, and therefore intersections of $k_{0,x}$ and β occur at lower frequency or longer wavelength. **d)** Summary of the results in parts (a-b) and (c). The dashed and dotted lines identify the angular positions of the dips in the reflectance curves from (a) and (b). The black solid line corresponds to the intersections between the dispersion curves in (c), signifying coupling to SPPs.

Our simple structure comprises 10 nm of evaporated Au on top of an SiO_2 wafer [Fig. 3-2 (a)]. Using the transfer-matrix method, we calculated angle-dependent reflectance from air for slightly different wavelengths (7.45, 7.56, and 7.67 μm) corresponding to different values of n_{ox} (0.9, 0.84, and 0.76, respectively) [Fig. 3-2 (a)]. The local minima in the reflectance are evidence of coupling to SPPs propagating along the SiO_2/Au interface and our calculation show for thinner gold films minima become deeper. The positions of these minima shift toward smaller incident angles for increasing wavelength, as expected from the dispersion of SiO_2 [Fig. 3-2 (a)]. Figure 3-2 (b) shows the corresponding experimental results, which are in good agreement with our calculations.

To verify that these minima in reflectance correspond to coupling to SPPs, we plotted the dispersion relation of single-interface SPPs [37] and the dispersion curves of the incident light — taking only the component of the incident wave vector along the interface — for several different incidence angles [Fig. 3-2 (c)]. Direct coupling to SPPs is expected to occur roughly when these curves intersect. It can be seen in the inset of Fig. 3-2 (c), which zooms in on the region where $n_{\text{ox}} < 1$, that for every angle there are two distinct intersections. Only the shorter-wavelength intersection ($\sim 7.5\ \mu m$) results in clear coupling to SPPs. The wavelength of the other intersection ($\sim 9\ \mu m$) corresponds to high losses in the SiO_2[Fig. 2-2 (b)], so the SPPs are almost immediately absorbed. In Fig. 3-2 (d), we converted the intersections in the dispersion to a plot of the predicted coupling angle versus free-space wavelength (solid line). This curve matches well with the actual measured and calculated coupling angles. The slight discrepancy may be a result of experimental uncertainty and the limitations of the SPP wave-vector equation, which assumes that both the metal and dielectric have semi-infinite thickness [37].

We also examine the effect of the gold thickness, d, on the coupling between free-space light and SPPs on the Au/SiO$_2$ interface of the structure in Fig. 3-2 (a). In Fig. 3-3, we show the calculation performed for Fig. 3-2 (a), but for several values of d. By decreasing d, the dips corresponding to coupling to SPPs become deeper. Critical coupling appears to be reached for $d \sim 2$ nm, indicating that for $d = 10$ nm the system is heavily undercoupled; this explains why the dips in Fig. 3-2 (a, b) are so shallow.

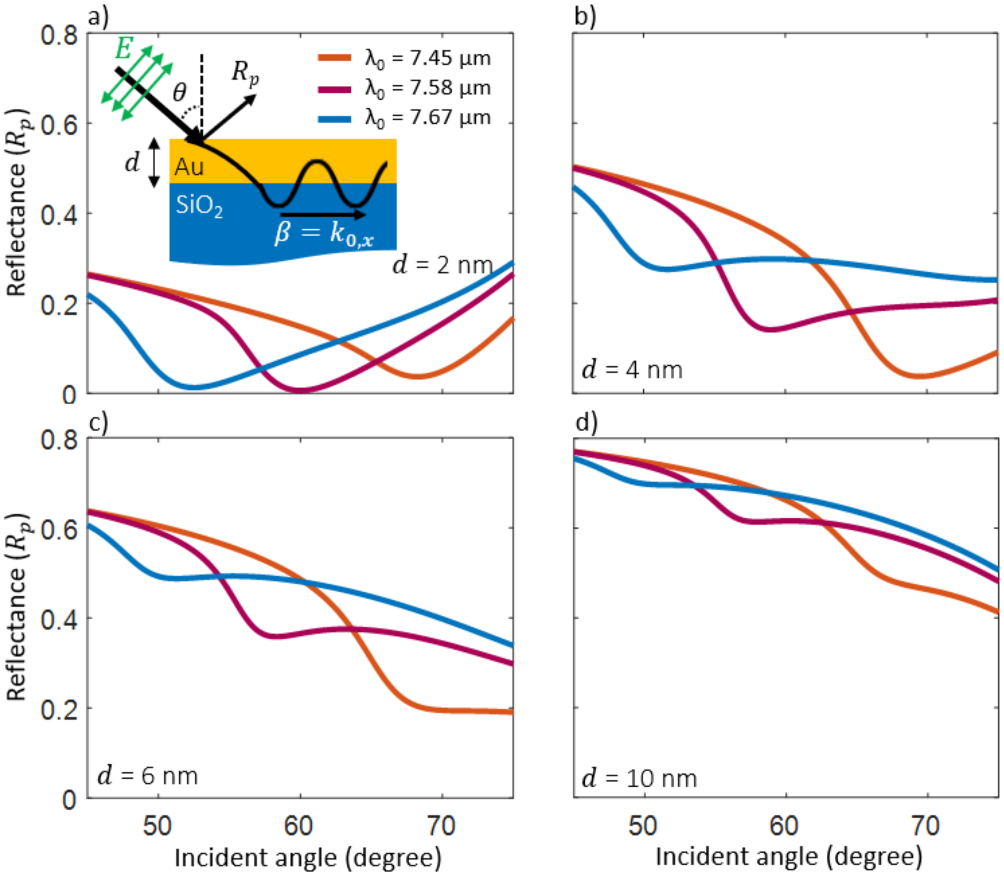

Figure 3-3) Effect of gold-layer thickness, d, on direct coupling to SPPs

(a) $d = 2$ nm, (b) $d = 4$ nm, (c) $d = 6$ nm, and (d) $d = 10$ nm. Note that (d) displays the same data as Fig. 3-2 (a).

3. Otto Configuration

Around a wavelength of 10 µm, amorphous Al_2O_3 has $n < 1$ and modest optical losses, represented by a small extinction coefficient, κ, as shown in Fig. 3-4 (a-b) [42]. Using these optical properties and the refractive index of aluminum, we calculated angle- and polarization-dependent reflectance for a 1-µm-thick layer of amorphous Al_2O_3 on an optically thick aluminum substrate using the transfer-matrix method. The thickness of the Al_2O_3 layer is approximately one tenth of the target free-space wavelength for our polarizer (free-space wavelength of 10.6 µm). Figure 3-4 (c) shows our calculation of the angle-dependent reflectance of this Al_2O_3/Al structure for both p- and s-polarized light (R_p and R_s). R_p approaches zero around an incident angle of 65° for a wavelength of 10.2 µm due to coupling to SPPs, while R_s remains close to unity for all wavelengths and angles.

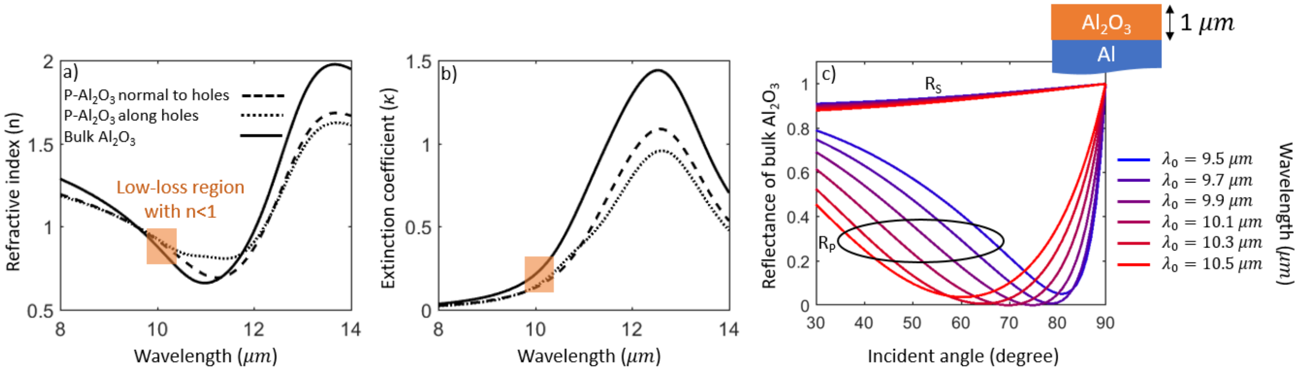

Figure 3-4) refractive indices and reflective behavior of Al_2O_3

(a) Real (n) and **(b)** imaginary (κ) parts of the complex refractive index of bulk (non-porous) amorphous Al_2O_3 (solid) [42] and porous anodic aluminum oxide (p-AAO), for polarization along (dotted) and perpendicular (dashed) to the p-AAO holes. The p-AAO calculation is based on Maxwell-Garnett effective-medium theory [43]. **(c)** P- and s-polarized calculated reflectance for a 1-µm-thick layer of amorphous Al_2O_3 on top of a thick aluminum film for the wavelength range in which Al_2O_3 has refractive index less than one and moderate loss.

Since our target wavelength was 10.6 µm rather than the ideal operating wavelength of 10.2 µm for the structure in Fig. 3-4 (c), we performed several calculations to identify an appropriate geometry. Our primary degrees of freedom were the Al_2O_3 thickness and porosity, though we also had some flexibility with the incident angle. In particular, increasing the porosity (density of air inclusions) of the Al_2O_3 is expected to bring the refractive index closer to that of air and reducing optical loss, resulting in coupling to SPPs at a slightly longer wavelength compared to the simulations in Fig. 3-4 (c). Based on our calculations, we identified a porosity of approximately 0.35 as a candidate for a 10.6-µm polarizer.

To realize our structure without the use of expensive nanofabrication techniques, we relied on an electrochemical anodization process to grow porous anodic aluminum oxide (p-AAO) with porosity of 0.35 on top of aluminum sheets (synthesis by InRedox LLC). Anodization can grow oxide layers on the surfaces of certain metals (aluminum, titanium, etc.), and is often used to enhance surface durability or for decorative purposes [44].

Figure 3-5 (a) shows scanning electron microscope (SEM) images of the resulting p-AAO. Similarly to p-AAO in the literature [44], the pores are cylindrical all the way through the oxide film. Here, the diameter of the pores is approximately 100 nm, which is much smaller than our working wavelength. Based on the SEM images, we modeled the optical properties of p-AAO based on an effective-medium theory for anisotropic media [43]:

$$n_{||} = \sqrt{(1-p) \times n_{AO}^2 + p \times n_{air}^2}, \quad \text{Eq. 1}$$

$$n_{\perp} = n_{AO}\sqrt{\frac{2(1-p) \times n_{AO}^2 + (1+2p) \times n_{air}^2}{(2+p) \times n_{AO}^2 + (1-p) \times n_{air}^2}}. \quad \text{Eq. 2}$$

Here, p is the volume ratio of air and n_{AO} is the complex refractive index of bulk Al_2O_3. The real and imaginary parts of the anisotropic complex index for $p = 0.35$ are shown in Fig. 3-4 (a-b). We used these optical properties to model the reflectance of our polarizers. The calculated spectral reflectance for three different incidence angles for 1-µm-thick p-AAO with porosity of 0.35 on an aluminum substrate are shown in Fig. 3- 5 (b), indicating an efficiency of more than 90%.

We performed angle-dependent spectral measurements of the fabricated p-AAO/Al structures using the reflection mode of the J. A. Woollam IR-VASE Mark II ellipsometer, and found excellent agreement with the calculations [Fig. 3-5 (b)]. The reduction of the measured R_s value (~0.85) compared to the calculations (0.95) is assumed to be mostly due to scattering from inhomogeneities in the structure. Note in Fig. 3-5 (b) that the reflectance is highly dependent on polarization and it can be close to 0 for one polarization and close to 1 for another. In the next section, we explore this effect to realize a new type of optical polarizers.

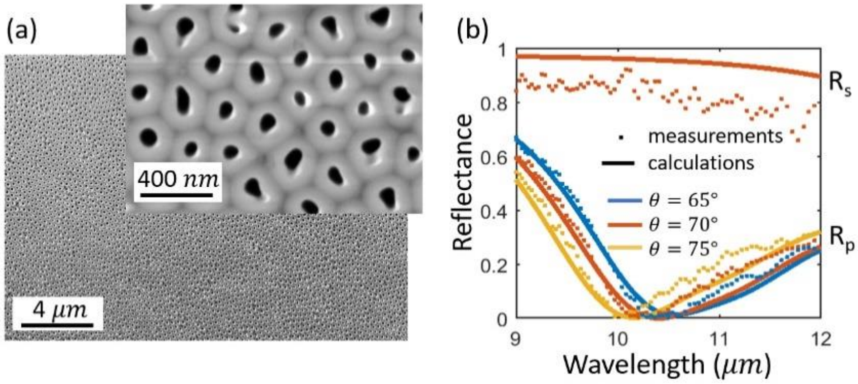

Figure 3-5) Scanning electron microscope of AAO and its reflective behavior

Scanning electron microscope (SEM) images of porous anodic aluminum oxide (p-AAO), imaged from the top of the sample. The inset SEM image of the same sample magnified 10 times. **(b)** Measured (dotted) and calculated (solid) spectral reflectance for p polarization, R_p, and s polarization, R_s, of a 1-µm layer of p-AAO on top of a thick aluminum film for the wavelength range in which Al_2O_3 has refractive index less than one. Different colors show incident light with different incident angles.

a. Polarizer based on direct coupling to SPPs

Optical polarizers typically function in transmission, reflection, or refraction modes. Wire-grid polarizers based on subwavelength parallel metallic wires transmit light with polarization perpendicular to the wire direction [45], [46]. Glan–Taylor prisms are refractive polarizers [47] that spatially segregate light with orthogonal linear polarizations. Reflective polarizers reflect light with a particular polarization; for example, Brewster-angle polarizers selectively reflect light polarized out of the plane of incidence (s polarization) [48].

The most common high-extinction-ratio polarizers in the long-wavelength infrared (LWIR) are based on finely spaced wire grids or other micro/nanostructures and are thus rather expensive optical components. In this section, we introduce an infrared reflective-type polarizer based on direct coupling between free-space light and a special type of surface-plasmon polariton (SPP) mode that has a dispersion relation above the light line. This approach requires no micro- or nanopatterning and can thus be inexpensively manufactured. We demonstrated such a polarizer based on porous anodized aluminum, designed to operate at CO_2-laser wavelengths.

Polarizers are readily evaluated using two figures of merit: extinction ratio and efficiency. The extinction ratio is the ratio of the output power to the input power, given input light polarized perpendicular to the desired polarization (i.e., in the “wrong” polarization). The efficiency is the ratio of the output power to the input power, given input light polarized along the desired polarization direction. Therefore, in Fig. 3-4 (c), R_s can be interpreted as the efficiency of a reflective polarizer based on direct coupling to SPPs, and thus we observe that such a polarizer can have efficiency (R_s) above 90%, with an extinction ratio (R_s/R_p) approaching infinity as R_p approaches zero.

The extinction ratio and operational bandwidth of our proposed polarizer can be increased by having two or more p-AAO/Al samples positioned next to each other in a way that the reflected light from the first one is incident on the second one, etc. [e.g., Fig. 3-6 (a)], though this decreases the efficiency of the resulting polarizer. We used a simple scheme called the K-geometry [49] which has a mirror between two samples to guide the reflected light from the first sample to the next (the mirror can also be replaced with another p-AAO/Al sample). This scheme results in a polarizer that maintains the position and directionality of an incident beam, so it can be incorporated into the path of a laser beam without affecting any other optical components [Fig. 3-6 (b)]. Note that by slightly rotating the orientation of the individual films, the total operational bandwidth of the polarizer can be increased, albeit with a reduction in the extinction ratio.

To test the operation of the proposed polarizer, we 3D printed a box [Fig. 3-6 (b)] that holds two p-AAO/Al samples like those in Fig. 3-5, designed to function as polarizers at an incident angle of 70°, for wavelengths corresponding to CO_2 laser emission (10.2 to 10.7 μm) [50]. We measured the reflected light using only one p-AAO/Al sample in the box for p- and s-polarized light [Fig. 3-6 (c-d)], using two metallic mirrors to guide the light without changing the direction or position of the beam from the input to the output. The corresponding wavelength-dependent extinction ratio (R_p/R_s), both theoretical and measured using a CO_2 laser with power of approximately 200 mW, is shown in Fig. 3-6(e).

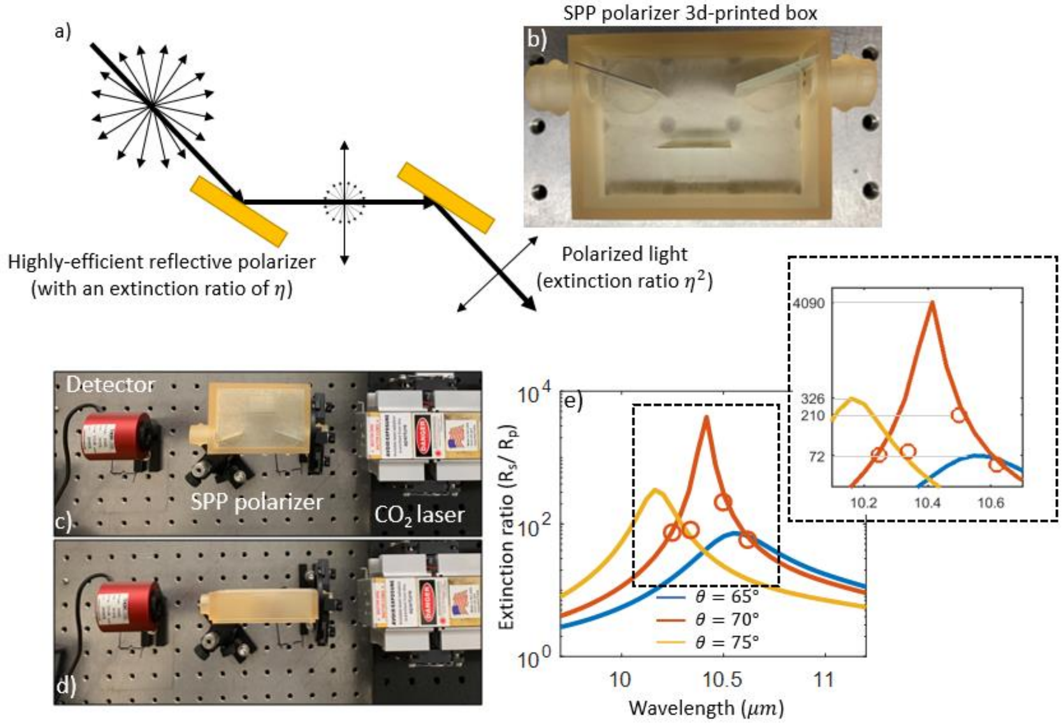

Figure 3-6) experimental setup and data of our polarizer using CO_2 laser

Increasing the extinction ratio or operational bandwidth of our SPP polarizer by placing two samples next to each other **(a)** without using a mirror, **(b)** by using a mirror, resulting in conservation of beam position and direction. **(c-d)** Testing of the polarizer box shown in (b), but with a single p-AAO/Al sample and two metallic mirrors (i.e., here we are not stacking the p-AAO/Al polarizers). Measurements were performed with a CO_2 laser for two different orientations of the polarizer. **(e)** Calculated (lines) and experimental (circles) extinction ratios (R_s/$R_{p,}$) using the setup in c, d.

b. Anodization process and coupling to SPPs in porous samples

We used anodization, an electrochemical process, to synthesize our porous aluminum oxide (p-AAO) on aluminum sheets. The process converts metallic surfaces into oxide layers resulting in more durable and corrosion-resistant surfaces. The resulting oxide layer becomes uniformly porous at certain growth conditions (chemistry, current, temperature, etc.). We found that a p-AAO layer with porosity of 0.35 and thickness of 1 micron can be a good candidate for our polarizer. This finding is a result of various thin-film calculations and measurements using many different samples with different porosities purchased from InRedox LLC to validate our modeling.

In general, increasing the porosity results in a red shift of the coupling wavelength according to our calculation based on the anisotropic refractive index of p-AAO. This is shown in the Fig. 3-7, where larger porosity results in coupling at a longer wavelength. This happens because when the refractive index is less than one, introducing air voids shifts the refractive index to closer to unity.

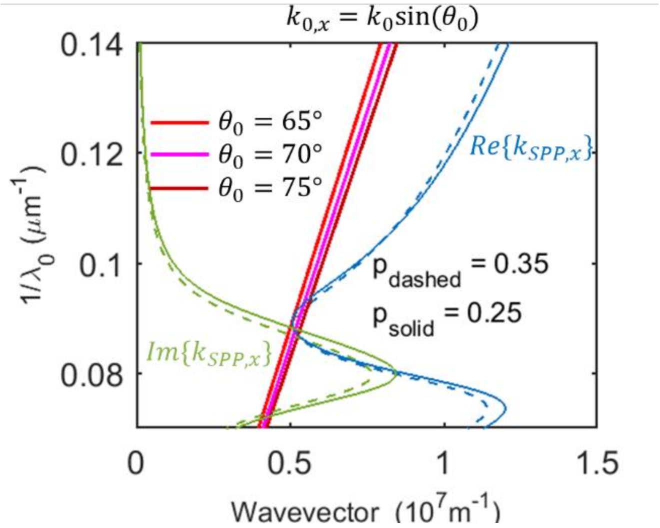

Figure 3-7) wavevector and angular frequency relation. Relation between the wave vector and the reciprocal of the free-space wavelength (i.e., the angular frequency) for surface-plasmon polaritons (SPPs) at the interface between Al and p-AAO for different porosity (dashed and solid lines are representative of 0.35 and 0.25 porosity, respectively). Three light lines show the $k_{0,x}$ component of the wave vector of the incident light for three different incident angles. The blue lines show the real part of $k_{SPP,x}$ and green lines show the imaginary part of $k_{SPP,x}$.

Figure 3-8 shows the wavelength and thickness dependence of the extinction ratio of the p-AAO/Al structure for different incident angles and porosities. Based on this figure, very high extinction ratios (> 1000) can be achieved. Increasing the porosity tends to push the region with high extinction ratios toward longer wavelengths and larger thicknesses. Increasing the incident angle tends to increase the extinction ratio.

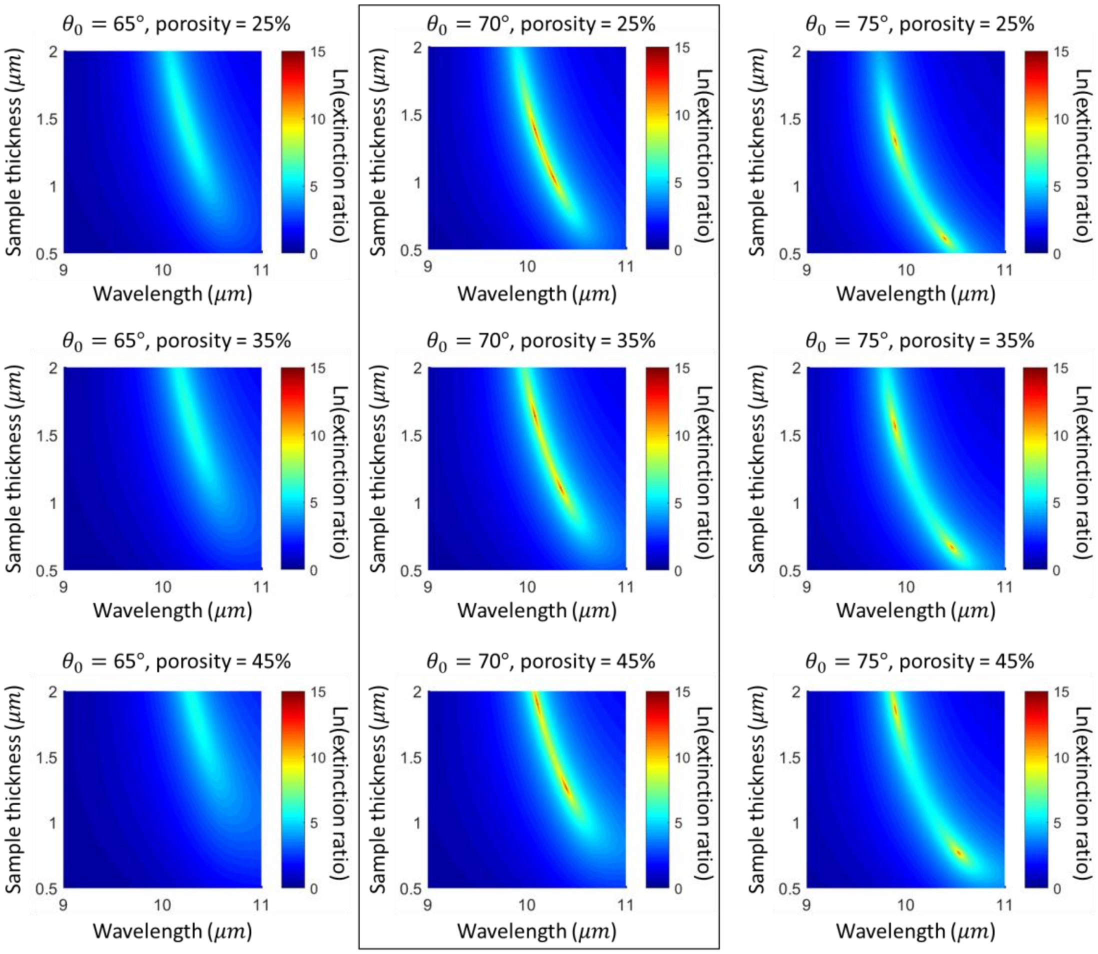

Figure 3-8) Calculated wavelength and thickness dependence of the extinction ratio of our sample

Furthermore, we conducted a calculation for a finer angular step size (from 65° to 75°, with step size of 1°) to investigate the difference between the calculations and our measurement using a CO_2 laser (Fig. 3-9). This calculation shows that the peak of extinction ratio has a large angular sensitivity. Thus, it is possible that some of the differences between the calculations and our measurements are a result of errors in the incident angle on the sample due to misalignment.

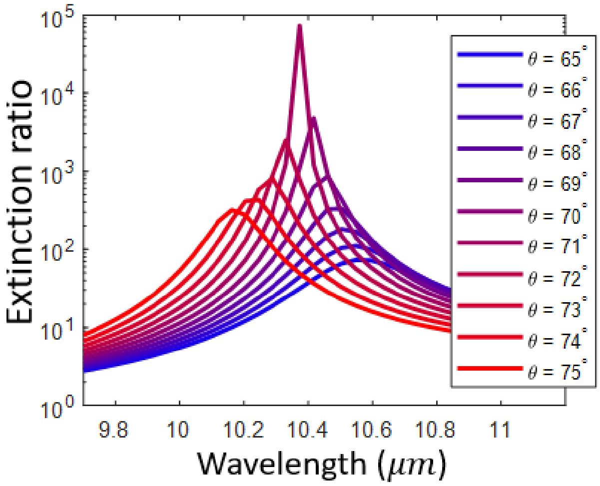

Figure 3-9) Calculated extinction ratio of our p-AAO/Al sample versus wavelength for incident angles from 65° to 75° with step size of 1°.

c. Using different dielectrics: covering other spectral ranges

To design SPP polarizers at substantially different wavelengths, different materials with refractive index less than unity must be used. Figure 3-10 (a) shows different candidate dielectric materials with refractive index less than one. In particular, we are plotting a figure of merit (FOM) that we defined as $\kappa/(1-n)$. Calculated results using two different dielectric materials with refractive index less than unity at two wavelength ranges, all on top of aluminum substrates, are shown in Fig. 3-10 (b-e). In Fig. 3-10 (b, c), we show that indium tin oxide (ITO) can realize polarizers in the near infrared. In Fig. 3-10 (d, e), we show that calcium fluoride (CaF_2) can be used for far-infrared polarizers.

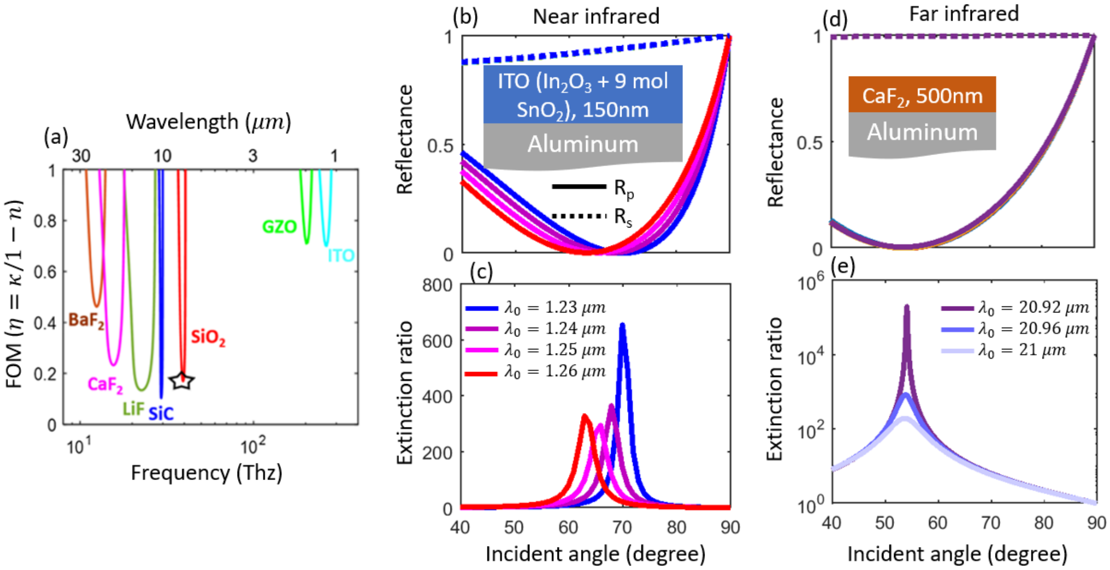

Figure 3-10) Covering other spectral ranges (a) Selection of other candidate dielectric materials with $n < 1$, including transparent conducting oxides in the near-infrared region and dielectric materials with strong vibrational resonances in the mid-infrared region. In all cases, the substrate is optically thick aluminum. (b) Reflectance and (c) extinction ratio of a near-infrared SPP polarizer based on a 150-nm film of indium tin oxide (ITO), with the optical properties from. (d) Reflectance and (e) extinction ratio of a far-infrared SPP polarizer based on a 500-nm CaF_2 thin film.

3. Conclusion

In this chapter, I presented our approach to coupling light directly into surface plasmon polaritons (SPPs) without the use of prisms, gratings, or similar approaches—and instead exploiting a material with refractive index less than one. Using this approach, we demonstrated a highly efficient reflective polarizer with a high extinction ratio that can be implemented in cheaper ways compared with existing commercial infrared polarizers. This polarizer relies on refractive index less than unity, and that is intrinsically narrow band. However, by stacking few samples with different spectral response (Fig. 3-10), we can achieve broader bandwidth. Also, we show in our CO_2 laser polarizer, one can achieve slight spectral bandwidth tuning by introducing air holes into the material with $n < 1$.

Chapter 4. Spectral and thermal engineering of absorptivity/emissivity

Motivation

Thermal emission is the process by which all objects at non-zero temperatures emit light, and is well-described by the classic Planck, Kirchhoff, and Stefan-Boltzmann laws [51][52]. In this chapter, first, we introduce our demonstration of a large-area (centimeter-scale) nonresonant metamaterial that features near-unity frequency-selective absorption in the mid-infrared wavelength range. The metamaterial comprises a self-assembled porous structure known as an inverse opal, here made of silica. The structure's large volume fraction of voids, together with the vibrational resonances of silica in the mid-infrared spectral range, reduce the metamaterial's refractive index to close to that of air and introduce considerable optical absorption. As a result, the frequency-selective structure efficiently absorbs incident light of both polarizations even at very oblique incidence angles. The absorber remains stable at high temperatures (measured up to ~900 °C), enabling its operation as a frequency-selective thermal emitter. The excellent performance of this absorber/emitter and ease of fabrication make it a promising surface coating for passive radiative cooling, laser safety, and other large-area applications.

In the second section of this chapter, we showed another way of engineering the absorptivity/emissivity of a structure based on a phase-transition material. Typically, for most solids, the power of light thermally emitted from the surface increases monotonically with temperature in a one-to-one relationship that is a cornerstone of conventional wisdom in physics, and enables applications such as infrared imaging and non-contact thermometry [53][54]. In this project, however, we demonstrate how to violate the one-to-one relation by using a strongly correlated quantum material that undergoes a fully reversible, temperature-driven solid-state phase transition. The smooth and hysteresis-free nature of this unique insulator-to-metal phase transition enabled us to engineer the temperature dependence of emissivity to precisely cancel out the intrinsic blackbody profile described by the Stefan–Boltzmann law, for both heating and cooling cycles.

The material in this chapter has been published as A. Shahsafi, et al. Wide-angle spectrally selective absorbers and thermal emitters based on inverse opals." *ACS Photonics* 6.11 (2019): 2607 and A. Shahsafi, et al. "Temperature-independent thermal radiation." *PNAS* 116.52, (2019): 26402.

1. Spectral-selective absorber/emitter

a. Introduction

Electromagnetic-wave absorption based on metamaterials has been a rapidly growing motif in different research fields, including energy conversion [55] and thermoregulation [56]. At optical frequencies, engineered absorbers are used for stray light reduction in the visible range [57], [58], refractive-index sensing in the near-infrared range [59]–[61], and thermal emitters [62]–[65] in the mid-infrared range. To achieve high absorption, the reflection, transmission, and scattering must all be minimized; this can be realized by an absorbing structure or material that is impedance-matched to the incident medium [66].

Since the wavelength of optical-frequency electromagnetic radiation is on the order of hundreds to thousands of nanometers, typical engineered optical absorbers are comprised of nanostructured materials [67], [68]. At the same time, many applications require inexpensive large-area absorbers [69], [70], motivating designs that can be fabricated without the use of top-down lithography. Examples of such lithography-free absorbers include carbon nanotube (CNT) forests [57], [71], and lossy low-index films like polydimethylsiloxane (PDMS) [72].

In this section, we demonstrate a wide-angle large-area absorber with polarization-independent spectral selectivity, realized using a metamaterial based on inverse opals (IOs), which are highly porous structures obtained through assembly of colloids that serve as a sacrificial structuring agent for a background matrix material [73]. In IOs, the size and arrangement of the pores and the material composition (background matrix, as well as dopants and other inclusions) can all be engineered, creating a large design space. The pores are also interconnected and can be infiltrated with fluids [74], which may be relevant for dynamic tunability, sensing, or catalytic applications.[75]–[79]

The diameter of the templating colloidal spheres used for IOs is typically on the order of a few hundred nanometers. After selective removal of the colloids, the corresponding volume comprises an interconnected array of air pockets while the surrounding volume is the glassy matrix material. The resulting composite material thus has an effective refractive index close to that of air (in particular, using silica matrix material), as has been observed at visible frequencies [80]. In the mid-infrared range, the vibrational resonances of silica [41] introduce substantial optical loss, resulting in an absorbing metamaterial that is well matched to the refractive index of air, thus minimizing reflections at the interface between air and the IO film.

A scanning electron microscope (SEM) image of an inverse opal film with void size of 250 nm is presented in Fig. 4-1(a), showing the highly interconnected and porous structure. The high degree of ordering (which can be disrupted through the addition of salts in the assembly process) is unimportant for the functionality at mid-infrared wavelengths; however, it is convenient for the modeling of the effective refractive index, since the volume fraction of background matrix and voids is well known for a face-centered cubic (fcc) lattice, 26% and 74%, respectively [73]. We performed infrared variable-angle spectroscopic ellipsometry (J.A. Woollam IR-VASE Mark II) on a 2-µm-thick IO film on silicon and extracted its optical properties (Fig. 4-1 (b), (c)). To convert the measured ellipsometric parameters, Ψ and Δ [14] , into the effective refractive index and absorption coefficient, we modeled the IO thin film using the Bruggeman effective medium approximation [43]. We first focused on 1.8 to 3 μm, a spectral range in which SiO_2 is nearly dispersionless and its refractive index is well known [12], and fit to the fraction of air present in the film (i.e. the film porosity). The resulting fitted porosity is ~76%, which is very close to the theoretical value of the porosity based on the fcc structure of the opal assembly ($\sqrt{2}\pi/6 = 74\%$) [73]. Fixing the porosity at this value, we then fit the ellipsometric measurements in the wavelength range of 6 to 12 μm, in which silica has vibrational resonances. The resulting Kramers–Kronig-consistent fitted effective complex refractive index of the inverse opal film, $n_{IO} + i\kappa_{IO}$, along with the fitted values assuming no porosity are shown in Fig. 4-1(b, c). The void size of the IOs (~250 nm) is significantly smaller than the wavelength in the mid-infrared range, ensuring the validity of the effective-medium assumption [81]. For comparison, the optical properties of an amorphous SiO_2 thin film from literature [12] are also displayed in the same figure. The IO film has n_{IO} very close to one (n_{air} = 1), and a significantly reduced κ_{IO} (but non-zero) compared to the bulk amorphous SiO_2.

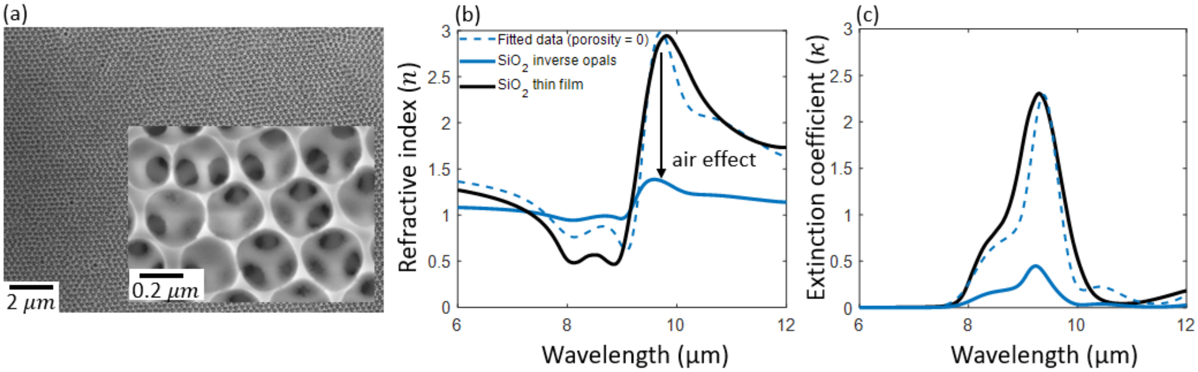

Figure 4-1) inverse opals structure and optical properties

(a) Scanning electron microscope (SEM) image of the inverse opals (IO) used in this study, showing the nano-porous and interconnected structure with a void diameter of 250 nm. The inset SEM image of the same sample with a 10 times higher magnification, showing the high porosity and interconnectivity of our IO sample. **(b)** Real (n) and **(c)** imaginary (κ) parts of the complex refractive index of the inverse opal film (solid blue lines) along with the fitted values assuming no porosity (dashed blue lines), and bulk sputtered amorphous SiO_2 (black lines) [19], for wavelengths close to the vibrational resonances of SiO_2. Optical properties of inverse opals are measured via variable-angle ellipsometry and fitted using the Bruggeman effective-medium theory [21].

Using the extracted refractive indices in Fig. 4-1 and the transfer-matrix method [15], [82], we calculated the optical impedance Z_{IO} of 2- and 4-μm thick IO film on a silicon substrate using the transfer-matrix method with the refractive index extracted from the ellipsometric data (Fig. 4-1). Figure 4-2(a) shows the magnitude of the difference between Z_{IO} and the free-space impedance, Z_0. We also calculated the impedance difference, $|Z_{\mathrm{ox}} - Z_0|$, between Z_0 and a homogeneous silica film of the same thickness on the same silicon substrate for the two thicknesses of 2 and 4 μm (Fig. 4-2(a), dashed lines). In a portion of the mid-infrared spectral range, the combination of the large volume fraction of air inclusions and the presence of strong vibrational resonances in silica results in a close match between the impedance of the IO structure and that of air; i.e., $|Z_{IO} - Z_0|$ approaches zero. We observed a large contrast between the $|Z_{\mathrm{ox}} - Z_0|$ and $|Z_{IO} - Z_0|$, especially near the vibrational resonances.

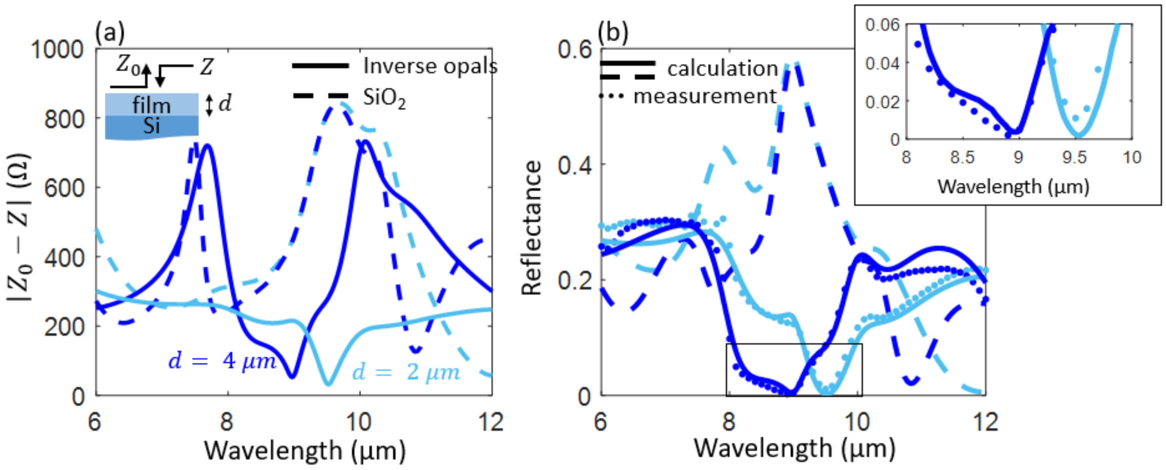

Figure 4-2) impedance of inverse opals

(a) The difference between the optical impedance of free space, Z_0 = 377 Ω, and the calculated impedance (using the transfer-matrix method), of a structure comprising a layer of IOs (Z_{IO}, solid lines) or homogeneous

SiO_2 (Z_{ox}, dashed lines) at two different thicknesses (2 and 4 μm), on top of a semi-infinite silicon substrate. **(b)** Measured (dotted) and calculated (solid lines) reflectance of the IO films, as well as bulk SiO_2 (calculated, dashed lines), at near-normal incidence. The reflectance of the IO film is suppressed due to impedance matching with air for wavelengths of 8 to 10 μm. The inset zooms in on the region of lowest reflectance.

To confirm the absorption around the resonances, we performed reflectance measurements using Fourier transform spectroscopy (FTS). Figure 4-2(b) shows the calculated (solid lines) and measured (dotted lines) values for the reflectance of the IO films at two thicknesses (2 μm and 4 μm) on top of a doped silicon substrate. The calculation was performed via the transfer-matrix method, using the optical properties extracted from ellipsometry [Fig. 4-1(b-c)]. The measurement was made using a Bruker Vertex 70 coupled to a Hyperion 2000 infrared microscope, with a numerical aperture of 0.4. As expected, the reflectance of the IO film becomes very small in the spectral region where the impedance is nearly matched to that of free space. In the same wavelength range, the reflectance of thin-film SiO_2 is quite large due to the large impedance mismatch.

We subsequently analyzed the angle-dependent reflectance of two IO films of different thicknesses (2 and 4 μm, as before) on silicon, for both s and p polarizations (Fig. 4-3). For both thicknesses, the reflectance decreases to nearly zero close to the spectral position of the vibrational resonances. Note that changing the film thickness affects the bandwidth of the suppressed reflectance region. Increasing thickness results in more light becoming absorbed in the spectral region where the IO film has a lower absorption coefficient.

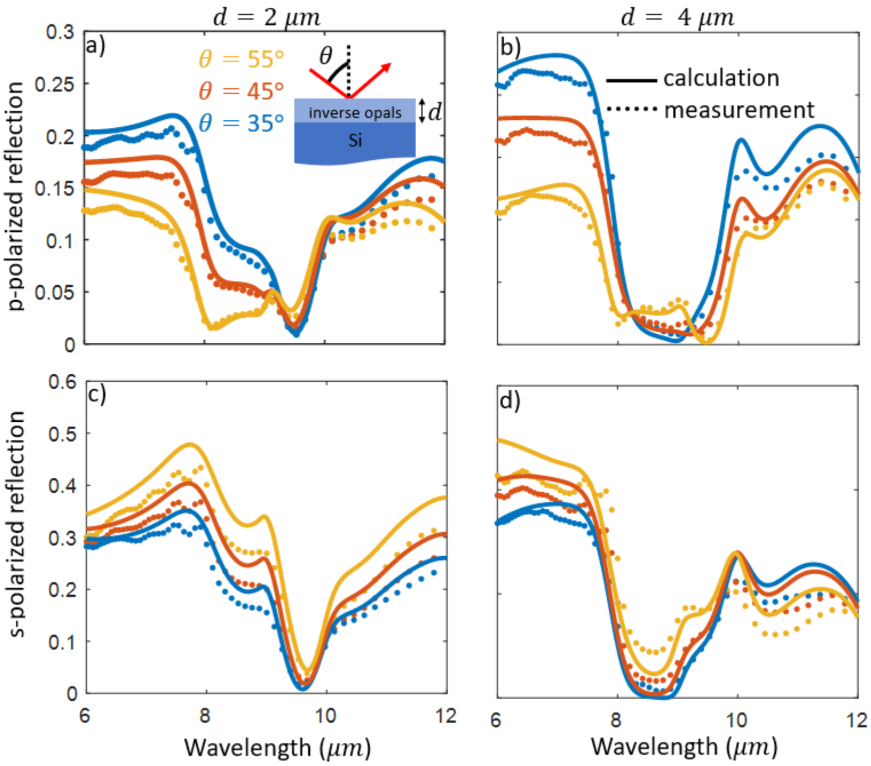

Figure 4-3) Reflective behavior of inverse opals at oblique incidence

Calculated (solid line) and measured (dots) reflectance at oblique incidence (θ = 35°, 45°, and 55°) for p- and s-polarized light for two different thicknesses of the inverse opal films (d = 2 and 4 μm).

The selective absorptivity of the IO structures implies that they can serve as a selective thermal emitters; this is encoded in Kirchhoff's law of thermal radiation, which equates the absorptivity at every wavelength (and angle and polarization) to the object's emissivity, assuming equilibrium conditions [65], [70]. Kirchhoff's law is also often used in the characterization of thermal emission from non-scattering samples, because it is frequently easier to infer absorptivity from reflectance and transmittance measurements than to directly measure thermal emission [83], [84]. For the samples in this work, however, it was difficult to apply Kirchhoff's law directly to the measurements because the semi-transparent silicon substrate was single-side polished, and the scattering from the back side is difficult to quantify.

To obtain accurate measurements of the emissivity, we performed direct emission measurements using FTS, as previously described in refs. [85], [86]. We collected the thermal emission from the samples at 150 °C and normalized it to the emission from a laboratory blackbody reference at the same temperature. The reference we used is a forest of vertically aligned CNTs (height = 0.5 mm) on a silicon wafer. We calibrated the emissivity of the CNT forest by comparing measured emission to the thermal emission from well-known flat wafers of fused silica and sapphire.

Using the direct thermal-emission technique, we measured the polarized oblique-angle emissivity by rotating the sample and placing a polarizer directly in front of it; this was done for s- and p-polarizations at three oblique angles [Fig. 4-4 (a, b)]. The accuracy of angle- and polarization-resolved direct thermal-emission measurements were confirmed by performing similar measurements on well-characterized flat wafers of fused silica and sapphire.

For further confirmation of the measurements, we calculated the expected emissivity of this structure using Kirchhoff's law and the extracted optical properties of the IO films in Fig. 4-1 (b-c). Two different emissivity spectra were calculated and presented in Fig. 4-4 (a-b); one set of curves corresponds to the structure's emissivity assuming zero transmission through the Si substrate, (*i.e.*, absorptance $A = 1 - R$ when $T_{\mathrm{Si}} = 0$), and the other assumes a lossless substrate (*i.e.*, $A_{\mathrm{Si}} = 0,\ A = 1 - R - T$). For the spectral regions where the IO film has relatively low loss ($\lambda < 8$ μm or > 10 μm), these calculations provide upper and lower bounds on the actual emissivity.

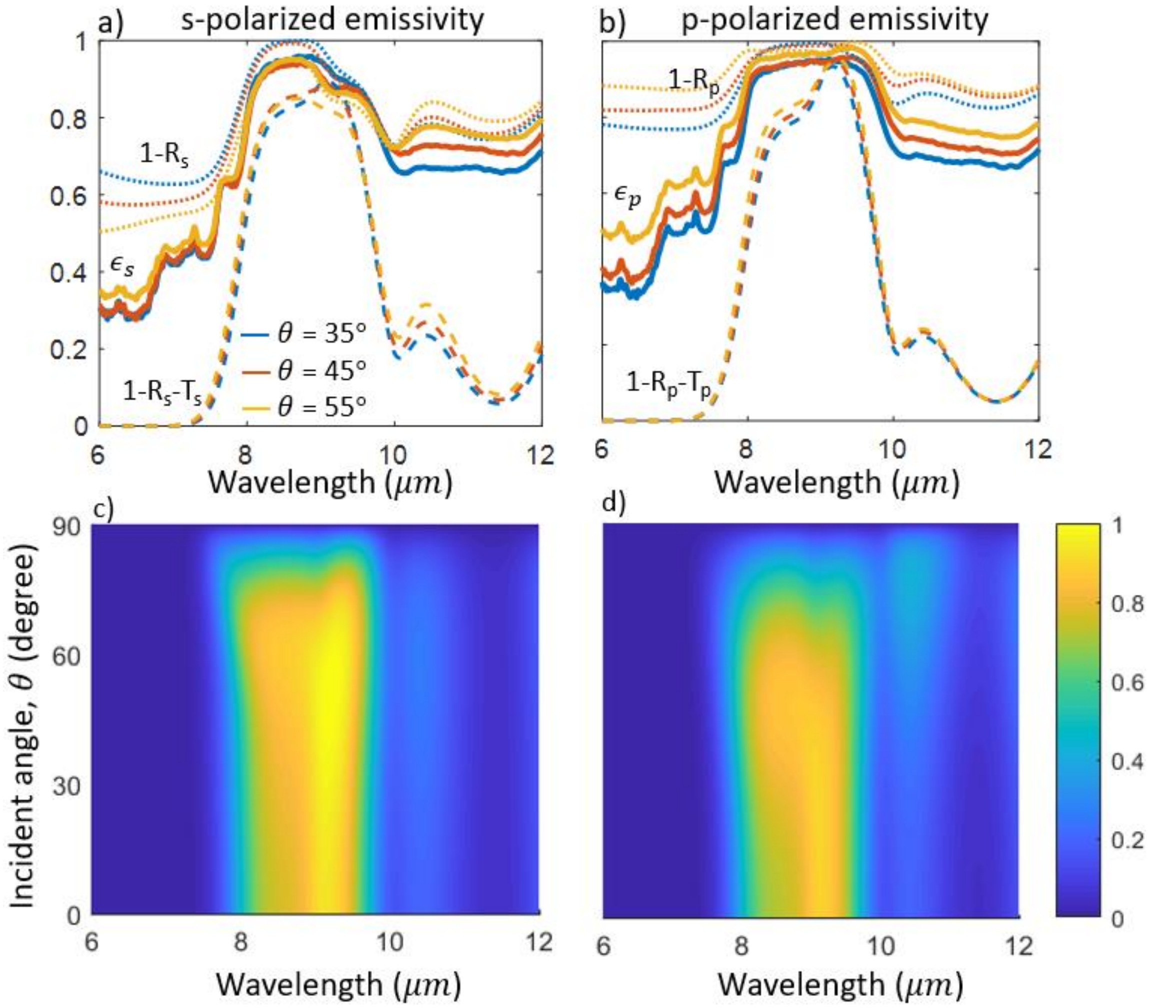

Figure 4-4) experimental and theoretical emission data of inverse opals

Experimental emissivity (solid lines) via direct-emission measurements at 150 °C for 4-μm-thick IO on silicon wafer at different incidence angles ($\theta = 0°, 35°, 45°$, and $55°$) for (**a**) s-polarized light and (**b**) p-polarized light, along with calculated upper and lower bounds on the emissivity in the spectral range where the IO film is low loss (λ < 8 μm or > 10 μm). In the spectral range where the IO film is low loss (λ <8 μm or >10 μm), we expect a substantial contribution to the emissivity from the lossy silicon substrate. Calculated absorption (1− transmission − reflection) within the film is shown versus wavelength and incident angle for (**c**) s polarization and (**d**) p polarization.

The large-area near-unity absorption at oblique incidence can be readily visualized using long-wave infrared ("thermal") imaging. Infrared-camera images typically attribute a pixel brightness to the intensity of detected thermal radiation from that pixel, assuming a constant emissivity for all pixels of the image. In Fig. 4-5, we show such infrared images of a silica glass slide (labeled “silica” in the image) next to the IO sample measured in Fig. 4-4, using a FLIR A325sc camera with a bandwidth of 7.5 to 13.0 µm. To isolate the high-emissivity region of the IO identified in Fig. 4-4, we positioned a filter with a passband of 8.2 to 10.6 µm in front of the camera. The infrared images with and without the filter can be seen in the bottom and top rows of Fig. 4-5, respectively, with the images taken from the normal direction, as well as for oblique angles of 35°, 45°, and 55°. These images demonstrate the large and broad-angle spectral selectivity of our selective thermal emitter. The “lines” of high apparent temperature seen on the bottom edge of the silica samples are a result of roughness (i.e., disorganized porosity, compared to highly ordered IO films), also resulting in enhanced emissivity.

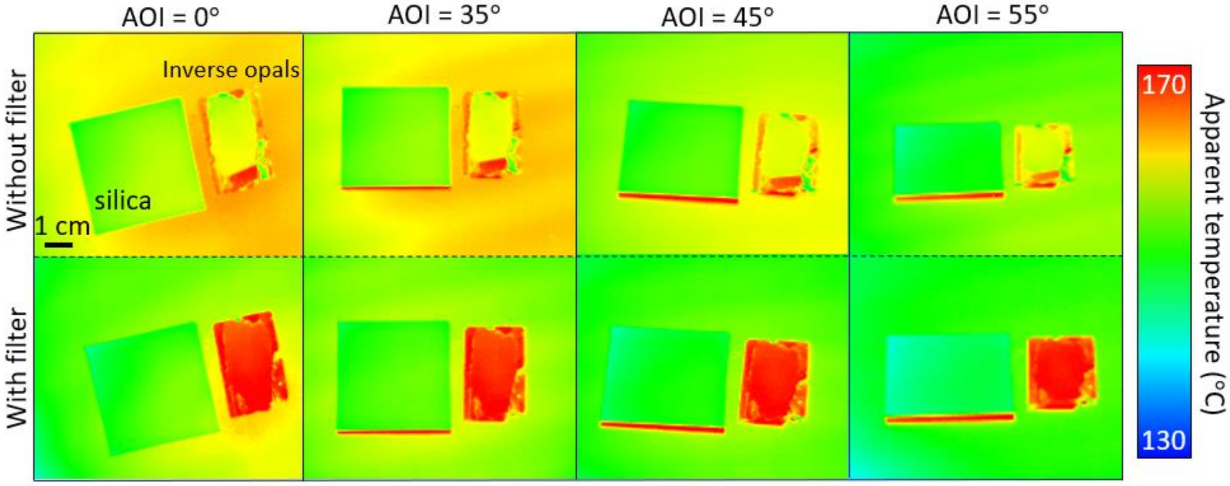

Figure 4-5) Mid-infrared images of the IO absorber with comparison with that of silica

Mid-infrared images of the IO absorber and a reference silica glass slide at 150 °C, imaged at angles (AOI) of 0 to 55°, with (top) and without (bottom) a filter that selects the wavelength range corresponding to high absorptivity/emissivity of the sample (8.2 to 10.6 µm). The close-to-unity emissivity of the IO absorber results in a large apparent temperature.

As a continuation of this work, our collaborators synthesized a few-microns-thick inverse opal film on a silica substrate to achieve a visibly transparent structure that is opaque in mid-infrared range. In the spectral range in which the emissivity of a flat silica surface is relatively low [Fig. 4-6(b)], the inverse-opal films can have high emissivity, and thus our new synthesized samples have a broadband infrared absorption while remaining visibly transmissive. Figure 4-6 (a) shows the spectral transmittance of this sample measured for both polarizations at oblique incidence angles using a variable-angle spectroscopic ellipsometer (J.A. Woollam IR-VASE Mark II) operating in transmission mode. We also measured the emissivity of this sample by measuring the spectral reflectance, R, of the sample using our FTS, and utilizing Kirchhoff's law to calculate the emissivity, ε, assuming light transmission and scattering are negligible in the mid-infrared range ($\varepsilon = 1 - R$). Both spectral emissivity of our sample and its substrate are presented in Fig. 4-6 (b). The emissivity of the flat silica substrate alone has a large dip around 9 μm, but the sample with an inverse-opal film on a flat silica substrate has high emissivity throughout the whole spectral region.

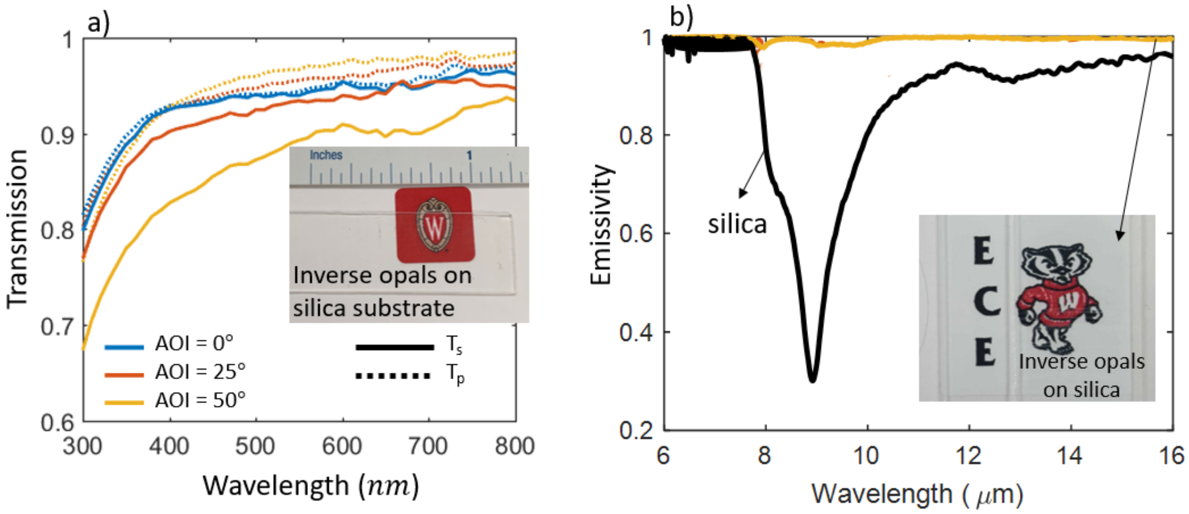

Figure 4-6) Visibly transparent infrared absorber. **(a)** spectral transmission of inverse opal film on silica substrate at oblique incidence for both polarizations. The inset shows an image of the sample, showing how visibly transparent it is. Inset shows the transparency of the sample **(b)** spectral emissivity of our sample (yellow trace), silica (black trace). The inset shows the transparency of the sample: the Bucky Badger logo is behind the sample.

b. Inverse opals synthesis

Our colleagues at Harvard synthesized inverse-opal (IO) films using an evaporative co-assembly method based on a procedure by Hatton *et al*. [73]. The templating colloids were monodisperse polystyrene particles with diameters ranging from 120 to 450 nm. Aqueous solutions of the colloids were synthesized by surfactant-free emulsion polymerization [87]. For co-assembly, we diluted these solutions to 0.1 v% particle content. They prepared the sol-gel precursor for the silica background matrix from a solution of 1.5 mL ethanol (100%, VWR), 1mL tetraethyl orthosilicate (TEOS, 98% Sigma Aldrich), and 1mL 0.1 M hydrochloric acid (HCl, Sigma Aldrich) solution, which was stirred at room temperature for one hour before use. The final co-assembly solution was prepared by adding 60 μL of the TEOS sol-gel solution to 12 mL of the colloid solution. For co-assembly, they used flat silicon substrates (approximately 1 by 4 cm). They prepared them by cleaning in piranha (3:1 sulfuric acid (Sigma): hydrogen peroxide (VWR)) for 30 min, washing in water and ethanol, and drying with compressed air. They suspended the substrates vertically in the co-assembly solution, which was then allowed to evaporate over 2 to 3 days at 65 °C. After the water fully evaporated, they produced the IO films by removing the colloidal template at 500 °C in air over 12 hours (5 h ramp time, 2 h at 500 °C, 5 h ramp back to room temperature).

The temperature stability of our inverse-opal sample was tested by heat-treatment in a high-temperature oven in air at 900 °C and 1100 °C for 120 min. Figure 4-7 shows the scanning electron microscope images of IO samples, showing that the structure survives the 900 °C anneal [compared to Fig. 4-1(a)], but does not survive the 1100 °C anneal.

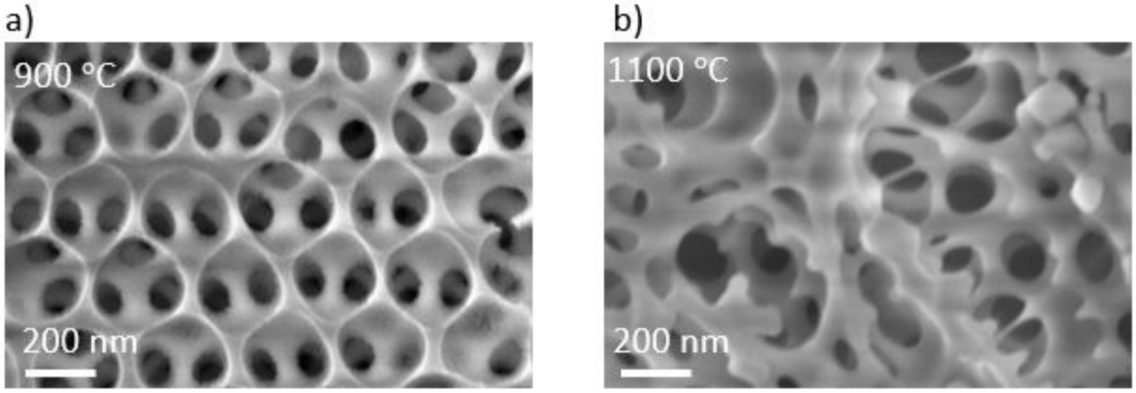

Figure 4-7) Scanning electron microscope (SEM) images inverse opals samples. These images are showing their structure is thermally stable up to 900 °C. The scale bar in both SME images are 200 nm

c. Ellipsometry measurement

Infrared spectroscopic ellipsometry measurements were performed on the synthesized IO films. Measurements were performed at three different angles of incidence: 35, 45, and 55°. Compared to infrared wavelengths, the feature size of IO films is very small, allowing the film to be modeled as a single effective medium. The films were modelled using an isotropic Bruggeman effective medium approximation ($p\frac{\epsilon_{eff}-\epsilon_{ox}}{2\epsilon_{eff}+\epsilon_{ox}} = (p-1)\frac{\epsilon_{eff}-1}{2\epsilon_{eff}+1}$, p is the volume fraction of the silica with permittivity of ϵ_{ox}) in which the composition of air and silica was tunable. The porosity used in this model is measured through near infrared ellipsometry. These parameters were then used in the longer wavelength infrared model of the IO film to fit a Kramers-Kronig-consistent oscillator model to the measured ellipsometry parameters Ψ and Δ. Experimental results and the corresponding fitted values are shown with dashed and solid lines in the Fig. 4-8, respectively.

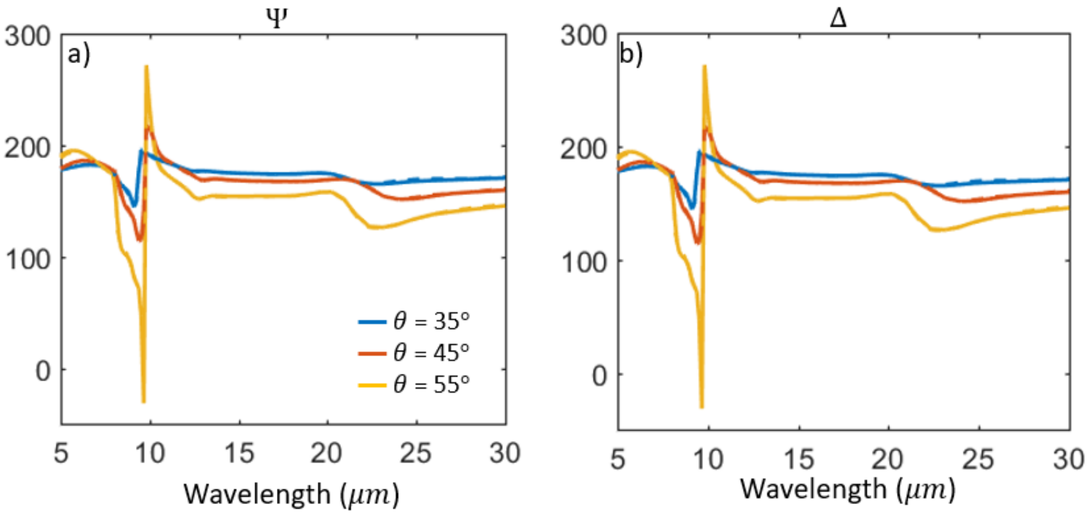

Figure 4-8) Fitted (dashed) and measured (solid) ellipsometry variables for inverse opals at three different incidence angles, θ, for (a) Ψ and (b) Δ.

2. Zero-differential thermal absorber/emitter

The total amount of power thermally emitted by a surface in free space can be obtained by integrating its spectral radiance—given by Planck's law and an emissivity—over all wavelengths and hemispherical angles [51] [52]. Assuming negligible angular dependence of the emissivity and wrapping the angular integral into the blackbody distribution, $I_{BB}(\lambda, T)$, this relationship can be expressed as:

$$A\int_{\lambda} d\lambda\, \varepsilon(\lambda,T) I_{BB}(\lambda,T) = A\varepsilon_{tot}(T)\sigma T^4, \quad \text{Eqn. (1)}$$

where A is the surface area, $\varepsilon(\lambda,T)$ is the spectral emissivity, λ is the free-space wavelength, T is the temperature, and σ is the Stefan-Boltzmann constant. For the vast majority of emitters, the total emissivity, $\varepsilon_{tot}(T)$, typically changes very slowly with temperature and is usually dwarfed by the T^4 term. Thus, the Stefan-Boltzmann law yields a one-to-one mapping between the temperature of an object and the emitted power, resulting in the conventional wisdom that hotter objects emit more light [Fig. 4-9 (a, c)].

This assumption of a near-constant emissivity must be re-examined for thermal emitters comprising materials whose optical properties can be widely tunable with temperature (i.e., thermochromics). For example, an emissivity that increases with temperature can result in emitted power growing faster than T^4 [88] [89], and an emissivity that rapidly decreases with temperature can overwhelm and reverse the slope of the typical Stefan-Boltzmann curve [90] [91].

In this section, we show that it is possible to achieve a complete breakdown of the conventional one-to-one mapping between the temperature and the thermally emitted power, P. A thermal-emission coating with this unique property can serve as a radiator that outputs a fixed amount of heat irrespective of its temperature, and can conceal differences in temperature across an object from infrared imagers. This condition can be written as $\partial P/\partial T = 0$, and occurs when $\varepsilon_{tot} = \gamma T^{-4}$, where γ is a constant with units of K^4. A surface with ε_{tot} that fits this form over some temperature range is henceforth referred to as a *zero-differential thermal emitter* (ZDTE). Achieving ZDTE behavior using real materials is extremely challenging: the necessary rate of change of the emissivity with temperature is much larger than what can be attained using conventional materials (e.g., with band semiconductors such as silicon, via temperature-dependent population of electrons to the conduction band, Fig. 4-9 (b)), but is smaller than that of materials with abrupt phase transitions (e.g., vanadium dioxide [90] [92]). Furthermore, this condition is only possible for a *hysteresis-free* temperature dependence of the emissivity, otherwise the ZDTE condition may only be satisfied during either heating or cooling, but not both.

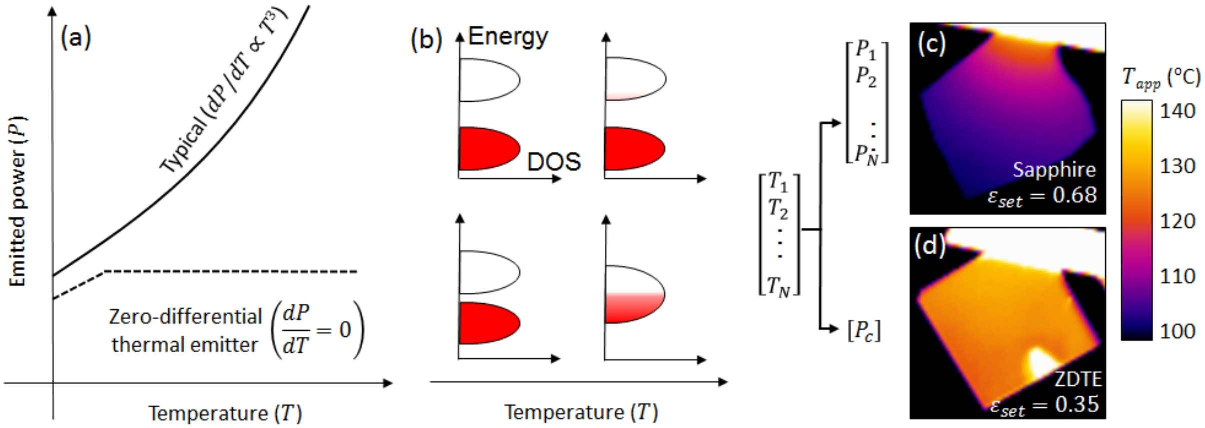

Figure 4-9) Thermal emission from a typical emitter (top part of the figure) and a zero-differential thermal emitter (ZDTE, bottom part of the figure).

(a, b) For a typical emitter, for example comprising a semiconductor or insulator (cartoon band diagram in (b), top), any change in emission from a temperature-dependent change in materials properties is dwarfed by the T^4 dependence in the Stefan-Boltzmann law. Conversely, a ZDTE decouples temperature and thermal radiation over some temperature range, and thus can only be made from a material with a very strong temperature dependence. In our implementation, we use the hysteresis-free insulator-to-metal phase transition in samarium nickelate ($SmNiO_3$) to achieve this behavior (b, bottom). **(c, d)** Long-wave infrared images of samples mounted to hang off the edge of a heater stage, such that a temperature gradient is established from hot (top) to cold (bottom). **(c)** a reference sample with a constant emissivity—in this case, a sapphire wafer—and **(d)** a ZDTE based on $SmNiO_3$.The color bar encodes the *apparent* temperature, obtained by assuming a particular set emissivity, ε_{set}, which was chosen such that the sample region just below the heat stage appeared to be at 130 °C, which is the actual temperature at that point (see more discussion in *Methods*). For sapphire, there is a one-to-one relationship between temperature and thermally emitted power. Conversely, the ZDTE exhibits a constant emitted power over a range of temperatures, here approximately 100 – 135 °C.

Here, we demonstrate ZDTE in the 8 – 14 μm atmospheric-transparency window using $SmNiO_3$, a correlated perovskite that features strong yet relatively gradual evolution of its optical properties over the temperature range of ~40 to ~140 °C, resulting from a fully reversible and hysteresis-free thermally driven IMT [93] [94]. The thermal IMT in $SmNiO_3$ is due to charge disproportionation in the Ni site and involves subtle changes in the Ni-O-Ni bond angle [95] [96]. In our $SmNiO_3$ films, this thermally-driven transition is reversible over many cycles, and has essentially no hysteresis in both electrical [Fig. 4-10 (a)] and optical measurements [Fig. 4-10 (b)], in stark contrast to many other materials with strong IMTs, e.g., vanadium dioxide [97]. We also see the same behavior in the electrical behavior of this sample as the transition of $SmNiO_3$ film deposited on sapphire substrates were studied by measuring their temperature dependent electrical resistance curves.

Hysteresis-free IMTs can be found in rare-earth nickelates with high phase transition temperatures, where negligible or complete absence of hysteresis may be due to the decoupling of the IMT with antiferromagnetic ordering, and faster phase-transformation kinetics at higher temperatures [98] [99]. The unique nature of this IMT is also directly observed in our spatially-resolved X-ray absorption spectroscopy (XAS) maps across the thermal transition [inset of Fig. 4-10 (a)], which demonstrate smooth variation with temperature (i.e., the absence of any metallic/insulating domain texture at any temperature) down to a ~20 nm length scale, including for temperatures deep within the IMT. No spatial features other than detector noise were observed. The trend in these spatial maps suggests a smooth crossover from the insulating limit to the metallic one, which is accompanied by a homogeneous phase landscape.

To enable design of thermal emitters using $SmNiO_3$, we performed temperature-dependent variable-angle spectroscopic ellipsometry over the 2 – 16 μm wavelength range, through the entire range of the phase transition [Fig. 4-10 (c, d)]. The resulting complex refractive-index data is consistent with the film becoming gradually more metallic from room temperature to ~140 °C. We note that while gradual transitions are generally considered to be less useful than abrupt transitions for electronic and optical switching technologies, here the gradual and hysteresis-free nature of the IMT in $SmNiO_3$ is essential for realizing ZDTEs. Also, for range of temperature that the $SmNiO_3$ undergoes phase change (*i.e.,* T = 40° to T = 140°) ellipsometry variables – Δ and Ψ – as a function of wavelength are provided in Fig. 4-11. These variables are measured using variable-angle spectroscopic ellipsometry (J. A. Woollam, Co. IR-VASE) and through these values n and κ are derived (Shown in Fig. 4-10). While the solid lines show the result of fitted model, dotted traces represent the experimental values of Δ and Ψ from ellipsometry measurement.

To create robust and large-area ZDTEs while minimizing fabrication complexity and cost, we explored designs based on un-patterned thin films of $SmNiO_3$. We used the temperature-dependent optical properties in Fig. 4-10 (c, d) and well-established optical thin-film calculations [100] to find the necessary combination of thickness of a $SmNiO_3$ film and a substrate that supports $SmNiO_3$ synthesis (Fig. 4-10 (a)) to achieve ZDTE over the 8 – 14 µm atmospheric transparency window. In Fig. 4-12 (a), we plotted the calculated temperature derivative of the emitted integrated radiance for several thicknesses of $SmNiO_3$ on sapphire, which indicates that ZDTE can be achieved for $SmNiO_3$ thickness of ~200 nm or greater. The result does not change much for a thicker $SmNiO_3$ films, indicating that the optical properties of the substrate do not affect the emissivity, making $SmNiO_3$ a versatile surface coating that can be utilized for scalable technologies.

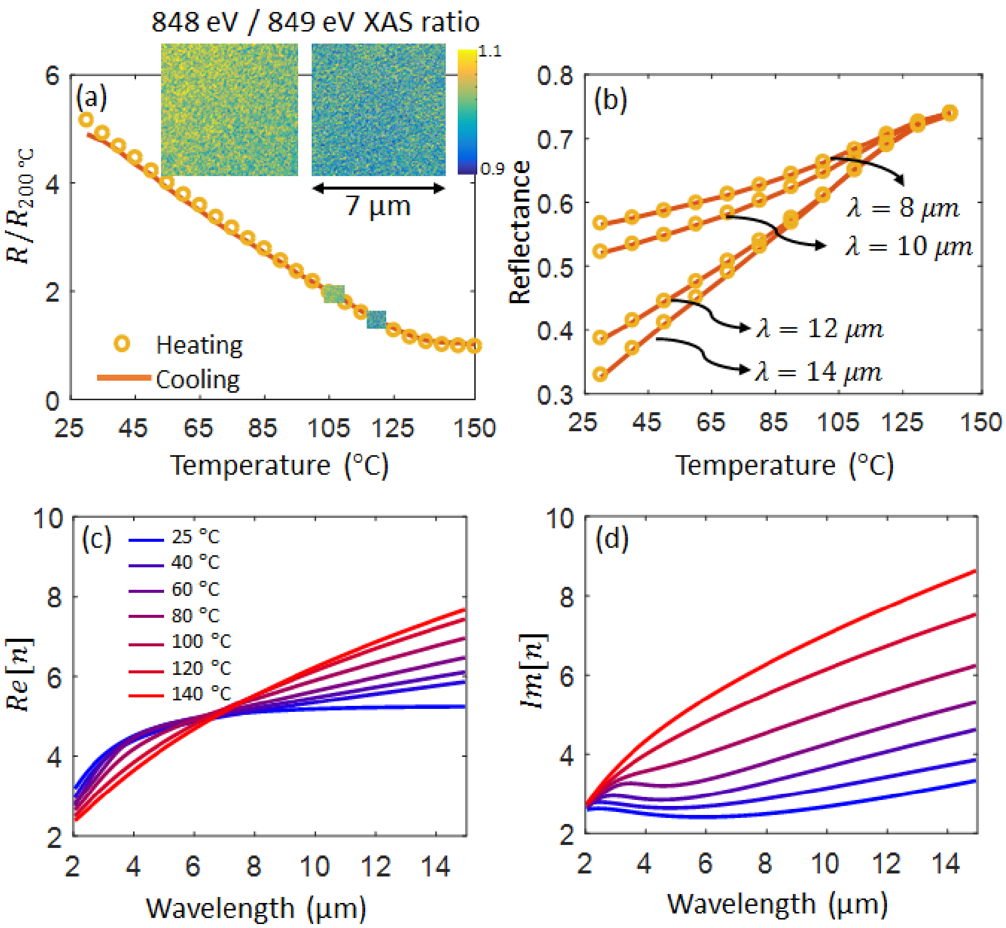

Figure 4-10) Electrical and optical behavior of $SmNiO_3$

(a) Normalized temperature-dependent electrical resistance of our $SmNiO_3$ thin film grown on a sapphire substrate and **(b)** mid-infrared reflectance at several representative wavelengths, during both heating and cooling, showing the hysteresis-free nature of the IMT in $SmNiO_3$. The insets in (a) are nanoscale x-ray absorption (XAS) maps at 105 and 120 °C, where the ratio of x-ray absorption at 848 eV to that at 849 eV is plotted as an indication of the metallic/insulating properties; no features other than detector noise are observed, indicating a gradual transition with no observable domain texture. **(c, d)** Temperature-dependent (c)real and (d) imaginary parts of the complex refractive index of the $SmNiO_3$ film, as a function of wavelength across the mid infrared, extracted using spectroscopic ellipsometry.

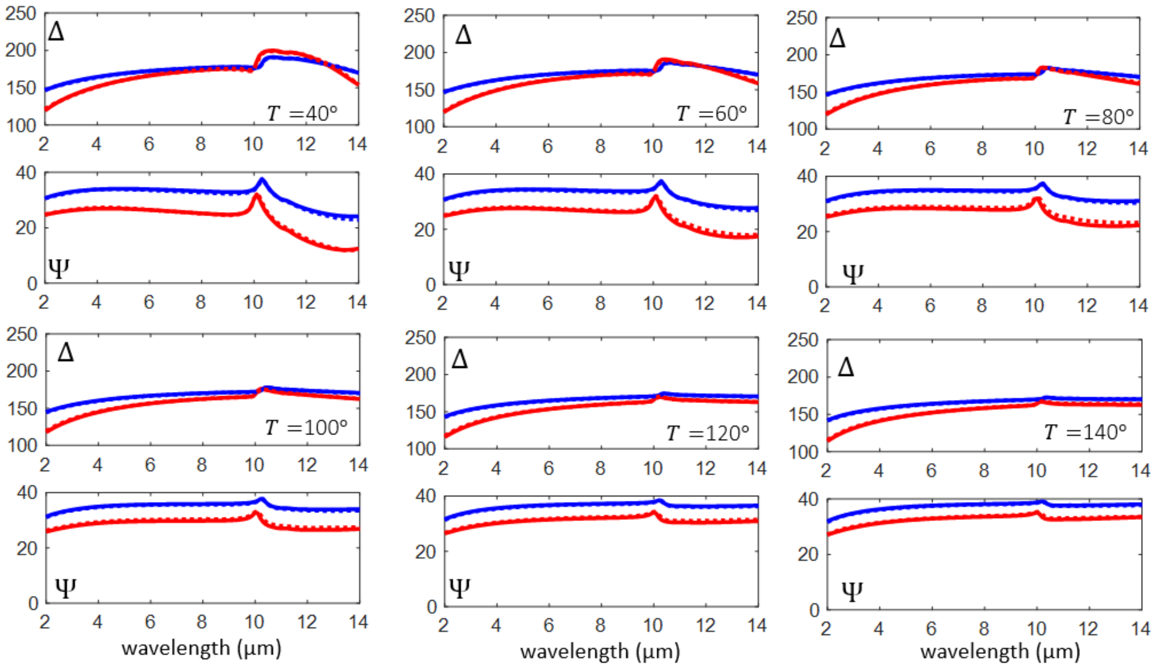

Figure 4-11) Spectral dependence of ellipsometry variables Δ and Ψ

Our fabricated planar device consists of a ~220-nm $SmNiO_3$ film grown on a *c*-plane sapphire substrate (Fig. 4-12 (a) inset), from which we measured the emissivity and the resulting thermally emitted spectral radiance. Because the resulting structure is opaque in our wavelength region of interest due to optical-phonon resonances in sapphire [101] and flat on the scale of the wavelength, Kirchhoff's law can be used to calculate the normal-direction emissivity $\varepsilon_N(\lambda, T)$ from normal-incidence reflection measurements: $\varepsilon_N(\lambda, T) = 1 - R_N(\lambda, T)$. We confirmed this result by measuring the thermal emission directly, normalizing to a laboratory blackbody consisting of a vertically-oriented 0.1-mm-tall carbon nanotube forest. Care was taken to isolate the sample thermal emission from the thermal background radiated by the various components of our instrument [102]. The results obtained from these two measurements are in excellent agreement [Fig. 4-12 (b)].

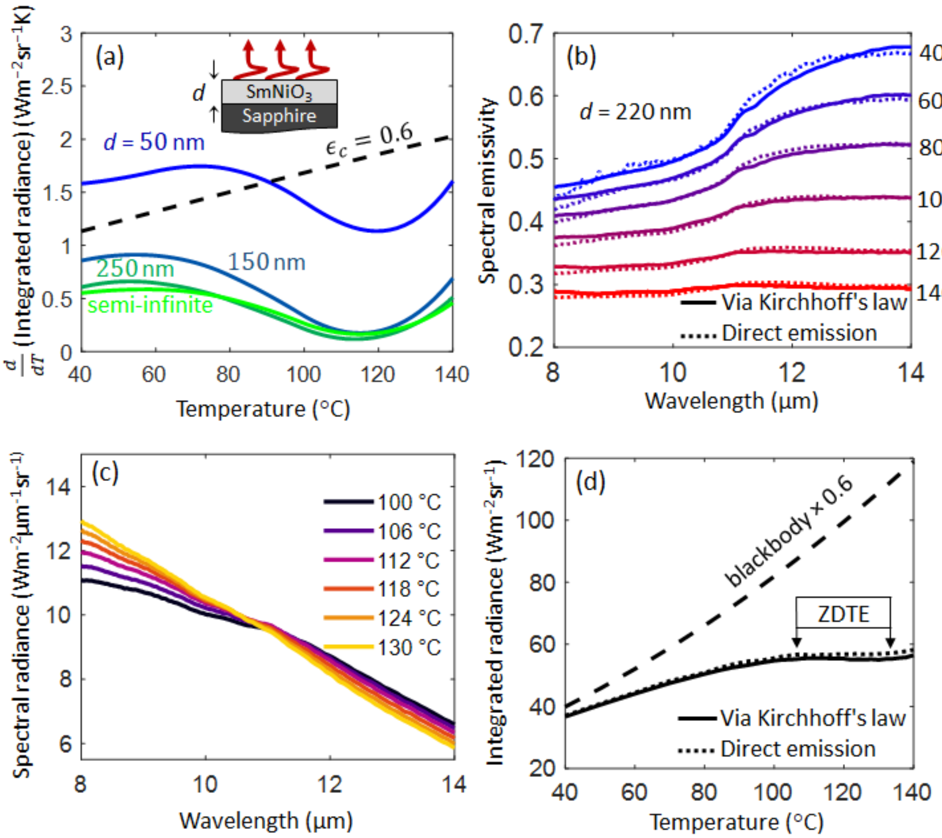

Figure 4-12) Zero differential thermal emitter

(a) Calculated temperature derivative of the emitted radiance, integrated over the 8-14 μm atmospheric transparency window, of an $SmNiO_3$ film with thicknesses d from 50 nm to infinity, on a semi-infinite? sapphire substrate. **(b)** Measured wavelength- and temperature-dependent emissivity of our ZDTE, comprising a ~220-nm film of $SmNiO_3$ on a sapphire substrate, via direct emission (dotted) and Kirchhoff's law using reflection measurements (solid). **(c)** The temperature-dependent spectral radiance of the ZDTE, which is the product of the spectral emissivity in (b) and the Planck distribution. **(d)** Thermally emitted radiance of our ZDTE, integrated over 8-14 μm, compared to that of a black body.

We integrated the measured spectral radiance [Fig. 4-12 (c)] over the 8–14 μm window to obtain the total thermally emitted integrated radiance as a function of temperature, which showed the desired ZDTE effect within a ~30 °C temperature window centered around ~120 °C [Fig. 4-12 (d)]. Away from the center of the phase transition of $SmNiO_3$, *i.e.*, below ~80 and above ~140 °C, the radiance vs. temperature profile becomes monotonic, as expected for a typical non-thermochromic thermal emitter.

The presence of the zero-differential region has profound implications for infrared imaging and control of infrared visibility. To demonstrate this, we performed a model experiment where two samples—our ZDTE, and a reference sapphire wafer—were mounted on a temperature-controlled chuck such that only a corner was touching the chuck and most of the sample was suspended in air, resulting in a temperature gradient from ~140 directly on top of the chuck to ~105 °C at the corner of the suspended area. When imaged with a long-wave infrared (LWIR) camera, the gradient is readily observable on the sapphire reference [Fig. 4-9 (b)], but almost completely disappears on our $SmNiO_3$-based ZDTE [Fig. 4-9 (c)]. The apparent temperature difference across the samples based on the camera image was ~34 °C for the sapphire, and ~9 °C for the ZDTE. The same phenomenon is observed in Fig. 4-13, where we show the temperature evolution of the infrared appearance of $SmNiO_3$-based ZDTEs compared to our laboratory blackbody reference (carbon nanotube forest), and sapphire and fused-silica wafers.

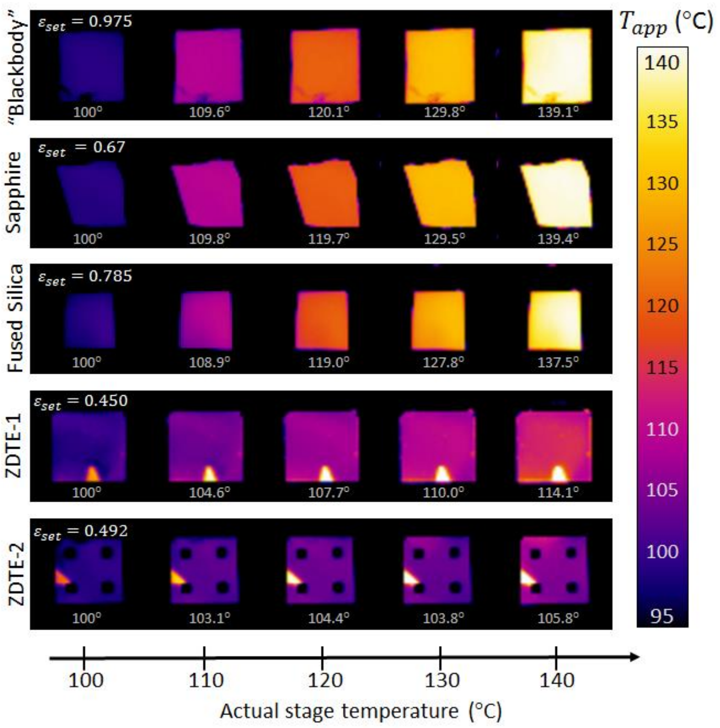

Figure 4-13) Long-wave infrared images of samples held at temperatures from 100 to 140 °C.

The emissivities of the laboratory blackbody (carbon nanotube forest), sapphire wafer, and fused SiO_2 wafer do not change appreciably over this temperature range. The emissivities of our $SmNiO_3$-based ZDTEs change as a function of temperature, and thus effectively mask the temperature differences from the camera. The apparent temperature is plotted [like in Fig. 4-6 (c, d)], with ε_{set} for each sample selected such that for a stage temperature of 100 °C , the infrared camera returned this value as the temperature reading. The dark squares on the bottom row are metal electrodes that were used for the resistance measurements in Fig. 4-7(a).

We note that the presence of zero-differential emission does not necessarily guarantee completely temperature-independent infrared signatures. For example, slight differences can still be observed in the emission from our ZDTEs at 110 °C vs. 140 °C in Fig. 4-13, resulting from a combination of effects that include imperfect cancelation of the blackbody curve and the change of the reflected light from the environment, since a change in emissivity coincides with a change in reflectance. The latter can be compensated during the design of ZDTEs by considering both the emitted and reflected light, assuming a particular background temperature. Furthermore, we presented calculated the angular performance of our camouflage device is investigated and it shows consistent behavior for oblique incident angle until 60° for both polarizations. Because sapphire is a birefringent material, we used Fresnel coefficient for birefringent materials to calculate angular response of our sample. The optical properties of sapphire for both axes are used and shown here in the Fig. 4-14 (a) from literature [101]. Utilizing the transfer matrix method, the thermally emitted radiance of our sample for both polarizations are presented in fig. 4-14. The calculated results for three oblique incidence angles as well as normal incidence show small dependency on the angular orientation of the sample.

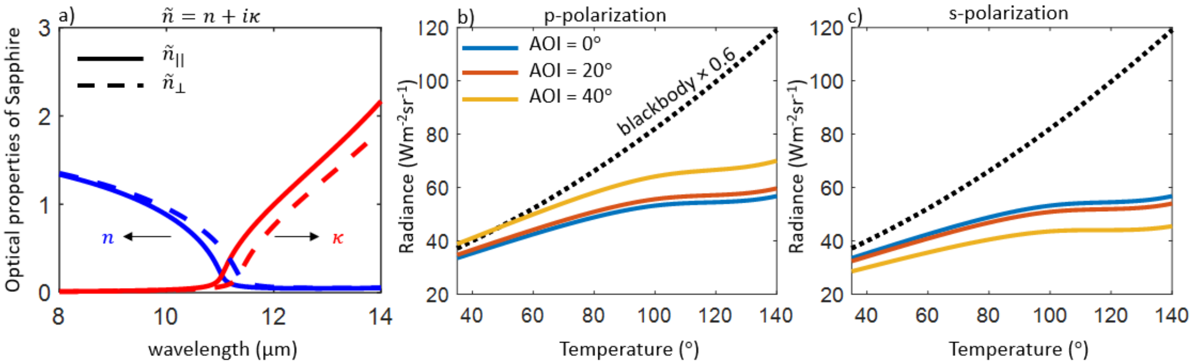

Figure 4-14) Calculated angular response of our sample. (a) Optical properties of sapphire for two both perpendicular and parallel axes, (b) p-polarization and (c) s-polarization radiance for oblique incidence (incidence angle = 0°, 20° and 40°)

3. Broad-band zero differential thermal emitter

As we discuss in the infrared imaging figure (Fig. 4-13), our zero differential thermal emitter's infrared camouflage performance is dependent on the bandwidth of the infrared camera/detector. For example, if one only looks at the thermal emission in the range of 8 to 11 μm, the dependence of thermally emitted power on temperature is roughly expected (i.e., an increase in the temperature results in higher thermal radiation). To address this limitation, we changed the substrate beneath of the SNO film. Based on some discussions with my advisor, we decided to introduce a substrate that had minimal spectral dependence (unlike sapphire, which has a sharp change in optical properties around $\lambda = 11\ \mu m$ [Fig. 4-14 (a)]) so that the resulting reflectance of the combination of the SNO film and the substrate had similar temperature dependence across the entire spectrum of interest.

Based on discussions with our collaborators at Purdue, we settled on indium tin oxide (ITO) as a compatible layer for SNO growth that does not have any feature in 8 to 14 μm range. Our collaborators then grew a 230-nm-thick SNO film on top of 110-nm-thick ITO film, on a silica substrate. The thicknesses were approximately selected based on thin-film calculations, but we did not view this as a rigorous optimization because we did not know the precise complex refractive index of the resulting ITO and the deposition process was untested, so the film growth rates were not well-known either. After the sample was fabricated, we performed direct-emission measurements using our FTS. Based on our calibrated thermal-emission measurements methodology [86], we measured the spectral emissivity of our new sample [Fig. 4-15(a)].

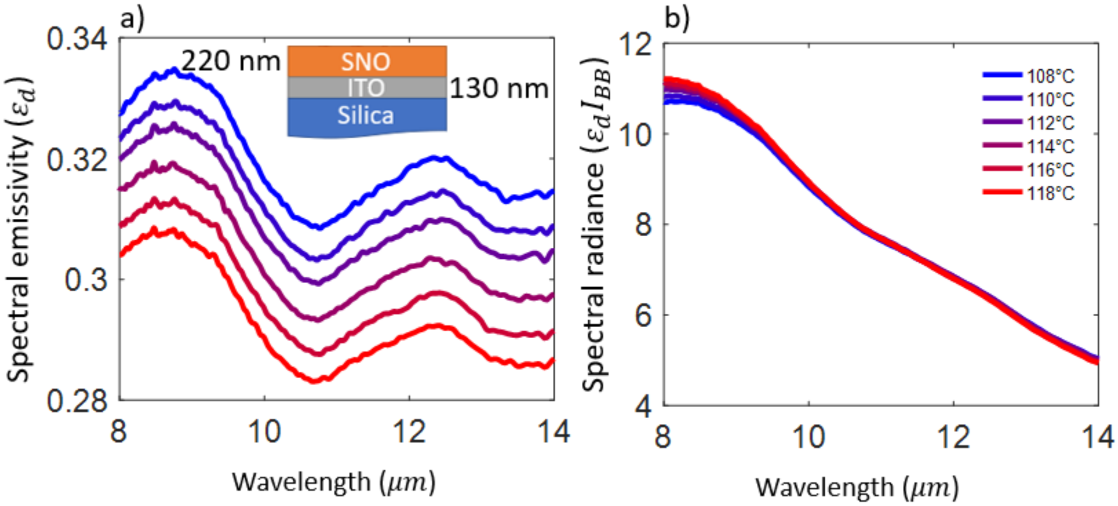

Figure 4-15) Broadband zero-differential thermal emission. **(a)** Wavelength- and temperature-dependence of the emissivity of our broadband zero-differential thermal emitter, $\varepsilon_d(\lambda, T)$, via direct emission of the shown sample, from 108 to 118 °C. (**b**) Temperature-independent spectral radiance, $I_d = \varepsilon_{BZDTE}(\lambda, T) \times I_{BB}$, showing broader spectral insensitivity compared to our previous work published in *PNAS* [103].

Figure 4-14 shows the emissivity of the sample along with its corresponding spectral, radiance which has very small temperature dependence from 108 to 118 °C, especially for wavelengths longer than 9 μm. We also conducted infrared imaging to confirm our spectral results on this sample using several optical filters in front of the camera. In Fig. 4-16, we show infrared images of our SNO sample on ITO/silica. Similar to Fig. 4-13, we place the sample on a heater stage, and increase the temperature gradually, and take infrared images at each temperature. By using a band-pass filter (8 to 10 μm), the difference between the apparent temperature (i.e., what the infrared camera reports) and the set temperature is larger compared to the case of without any filter. However, using a high pass filter (passing wavelength > 11 μm) results in smaller increase in the apparent temperature. This spectral infrared imaging agrees with spectral data in Fig. 4-15 (b): at shorter wavelengths, there is a noticeable difference in the thermally emitted power for different temperatures, but this difference is diminished for longer wavelengths.

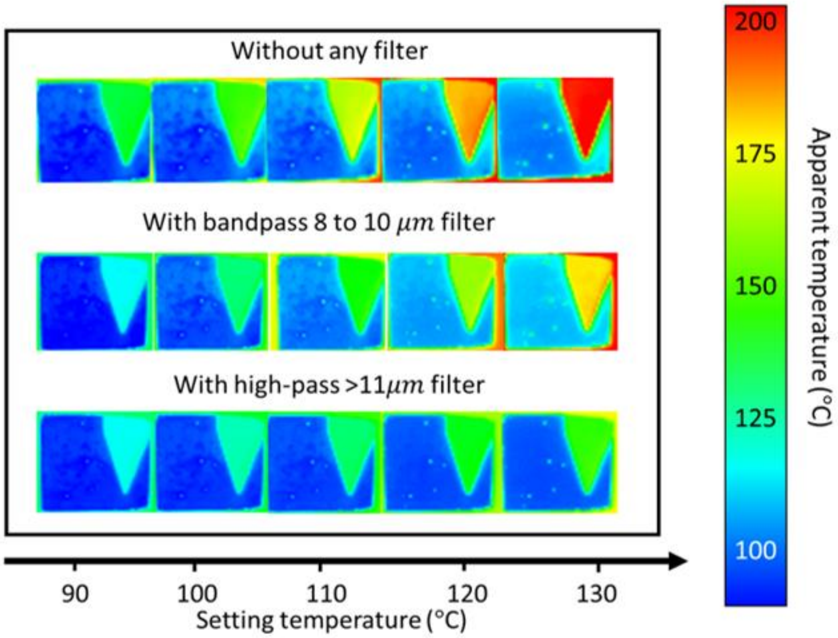

Figure 4-16) Filtered infrared imaging. Long-wave infrared images of an SNO/ITO/silica sample held at temperatures from 90 to 130 °C without and with two different spectral filters.

In conclusion, we demonstrated several ways to engineer the spectral emissivity of surfaces. First, we demonstrated a large-area, near-unity-emissivity mid-infrared absorber/emitter based on a self-assembled silica inverse opal (IO) metamaterial with a thickness less than half of the free-space wavelength. The device shows little angular and polarization dependence across its working wavelength of 8 to 10 μm, maintains a greater than 80% absorption for incident angles as large as 80°, and is stable up to at least ~500 °C. The broad-angle absorption is a consequence of impedance matching to the near-unity refractive index of the IO structure with considerable optical losses, resulting from the combination of mid-infrared vibrational resonance of the silica comprising the opal matrix and the large volume fraction of air inclusions.

Second, we presented our design results in temperature-independent thermally emitted power within the long-wave atmospheric transparency window (wavelengths of 8 – 14 µm) [104], across a broad temperature range of ~30 °C. The ability to decouple temperature and thermal emission opens a new gateway for controlling the visibility of objects to infrared cameras and, more broadly, new opportunities for quantum materials in controlling heat transfer. The ability to decouple temperature and thermal radiation with our simple design enables new approaches to conceal heat signatures over large areas, for example for wearable personal privacy technologies, and also has implications for thermal management in space. More broadly, this demonstration can motivate new areas of inquiry for quantum materials that possess highly tunable electronic structures.

Chapter 5. Conclusion

In this thesis, I described several demonstrations of new infrared optical phenomena enabled by low-index materials and phase transition materials, resulting in several devices that include reflective polarizers, optical absorbers, and infrared camouflage coatings. Specifically, using dielectrics with refractive index less than one, $n < 1$, we demonstrated superior reflectance compared to metal mirrors, investigated the phenomenon of frustrated total external reflection (an analog of frustrated total internal reflection). We anticipate that frustrated external reflection may be useful for, e.g., compact angular filters.

Moreover, in chapter 3, we demonstrated direct ways to couple to surface plasmon polaritons (SPPs), removing the bulky prisms in the Kretschmann and Otto configurations. Using nano-porous anodic aluminum oxide, we demonstrated very efficient reflective polarizers with high extinction ratios. Notably, our method does not require any nanopatterning or other expensive fabrication techniques, resulting in a low-cost design that can be easily mass produced. However, the significant angular and spectral sensitivity of this optical device requires stable and accurate alignment, and likely limits the utility of these polarizers to lasers and other narrowband light sources.

Using a recently developed self-assembly technique to synthesize silica inverse opals resulting in an index of refraction close to unity ($n \sim 1$), we showed how we can achieve spectrally selective but broad-angle absorptivity/emissivity. Through this platform, we demonstrated infrared large-area absorbers with high temperature stability, as described in chapter 4. By utilizing alternative matrix materials with a different set of vibrational resonances and/or by depositing materials within the IO voids, the self-assembly approach can enable large-area wide-angle absorbers and thermal emitters across the infrared range.

To further engineer emissivity of a sample in a reversible way, in the second section of chapter 4, we showed how to thermally engineer absorptivity/emissivity using a material that features a highly temperature-dependent refractive index, free of hysteresis. Through this platform, we achieved thermal camouflage that conceals thermally emitted information from infrared cameras, and envision thermally regulating surfaces that may passively maintain the temperature of a surface. Furthermore, using this platform, one can envision the design and implementation of adaptive neutral density filters such that that the optical density depends on temperature or other type of excitation.

Appendix A. Measurement of n_{ox} and κ_{ox} for SiO$_2$

For the bulk SiO$_2$ samples used in Section 5, optical properties were extracted using variable-angle spectroscopic ellipsometry (J. A. Woollam, Co. IR-VASE). The data was fit using a model comprising two Gaussian oscillators for the complex permittivity ($\epsilon = \epsilon_1 + i\epsilon_2$):

$$\epsilon_1 = \Gamma\left(\frac{E - E_n}{B_r}\right) + \Gamma\left(\frac{E + E_n}{B_r}\right) \tag{S.1}$$

$$\epsilon_2 = Ae^{-\left(\frac{(E-E_n)}{B_r}\right)^2} + Ae^{-\left(\frac{(E+E_n)}{B_r}\right)^2} \tag{S.2}$$

where A is the amplitude, E$_n$ is the center energy, and B$_r$ is the broadening of the oscillator. The function Γ produces a Kramers-Kronig-consistent line shape, and is defined in ref. [105]. The resulting fit parameters are shown in Table 1.

However, we were unable to use ellipsometry to extract the optical properties of our PECVD-deposited SiO$_2$ samples due to the need to preserve the polished backside surface for other measurements. Without roughening the backside of the sample, interference effects from that interface can substantially reduce the accuracy of ellipsometric modeling [1]. Instead, we determined the optical constants by reverse calculating the values from reflectance and transmittance measurements. We measured the angle- and wavelength-dependent reflectance and transmittance of our thinnest SiO$_2$ films (1.5 μm) on silicon, over the 7 – 9 μm range. We then used the transfer-matrix method [15] to calculate the corresponding reflectance and transmittance for an unknown film defined by a complex refractive index that we varied across the range of reported refractive index values for SiO$_2$ [42]. To determine which of these best corresponded to our films, we minimized the function $S(\lambda)$ for each wavelength λ, defined as:

$$S(\lambda) = \textstyle\sum_{\theta,s,p}(\delta_{(\mathrm{s,p}),\theta} + \Delta_{(\mathrm{s,p}),\theta}) \tag{S.3}$$

$$\delta_{(\mathrm{s,p}),\theta} \triangleq |R_{\mathrm{m},(\mathrm{s,p}),\theta} - R_{\mathrm{bf},(\mathrm{s,p}),\theta}|$$

$$\Delta_{(\mathrm{s,p}),\theta} \triangleq |T_{\mathrm{m},(\mathrm{s,p}),\theta} - T_{\mathrm{bf},(\mathrm{s,p}),\theta}|$$

where T_m and R_m are the measured transmittance and reflectance, T_{bf} and R_{bf} are the corresponding calculated values, s/p identifies the polarization, and $\theta = 35°, 40°, \text{and } 45°$ are the incident angles used. The resulting "brute-force-calculated" values of n_{ox} and κ_{ox} were then fit to the same Gaussian oscillator model, as shown in Table 1 and Fig. 5-1. The optical properties of our PECVD SiO_2 extracted using this method are also shown in Fig. 2-2 (dotted lines). As can be seen in Fig. 2-6, the calculated reflectance and transmittance using the extracted optical properties for SiO_2 matched reasonably well with the measurement even for incidence angles greater than 45° or other film thicknesses (3 or 6 μm SiO_2).

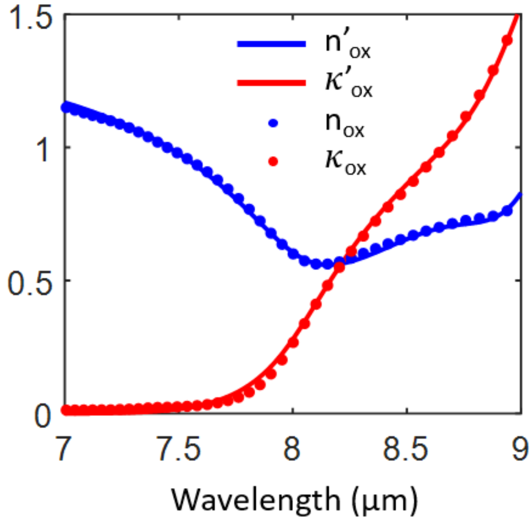

Figure 5-1) Optical properties of PECVD SiO_2 from fitting to a Gaussian model (n'_{ox}, κ'_{ox}) and from a wavelength-by-wavelength fit of the transmittance and reflectance data (n_{ox}, κ_{ox})

Table 1. Gaussian oscillator model properties for SiO_2 optical properties

	Amplitude, A		Center energy, E_n (cm^{-1})		Broadening, B_r (cm^{-1})	
Bulk SiO_2	10.55	1.01	1070.4	1092.2	63.58	228.63

PECVD SiO_2	7.92	1.65	1037.5	1105.5	81.66	193.2

Appendix B. Brewster angle and pseudo-Brewster angle

The Brewster angle is the angle of incidence for which there is no reflection of p-polarized light from an interface between two lossless transparent materials [25]. When light is incident onto a material with optical loss, such an angle does not exist, but there is still an angle for which p-polarized reflection is minimized, such that $\frac{d\left|r_p^2(\theta_{pB})\right|}{dt} = 0$; this is known as the pseudo-Brewster angle (θ_{pB}) [23]. θ_{pB} is shown in Fig. S2a for the case of light coming from air ($n_1 = 1$) and incident on an absorbing material described by some $n = \mathrm{Re}\{n_2\}$ and $\kappa = \mathrm{Im}\{n_2\}$. This figure shows that for large n_2 (*e.g.*, n and κ greater than 5), θ_{pB} is large (*e.g.*, greater than 60°). For the case of a noble metal in the mid infrared range, θ_{pB} is greater than 85°. The high-angle p-polarized reflectance of a gold mirror is plotted in Fig. S2-b for the mid-infrared wavelength range, showing a decrease of reflectance because of the pseudo-Brewster effect. The spectral and angular window in which SiO_2 has higher reflectance than gold is identified with a black box. The inset in this plot shows that p-polarized reflectance of SiO_2 surpasses the reflectance of Au at $\lambda = 7.4\ \mu m$ starting at an incident angle of 85°. This calculation was done using the transfer matrix method [105][107][106] and literature optical properties for gold [26].

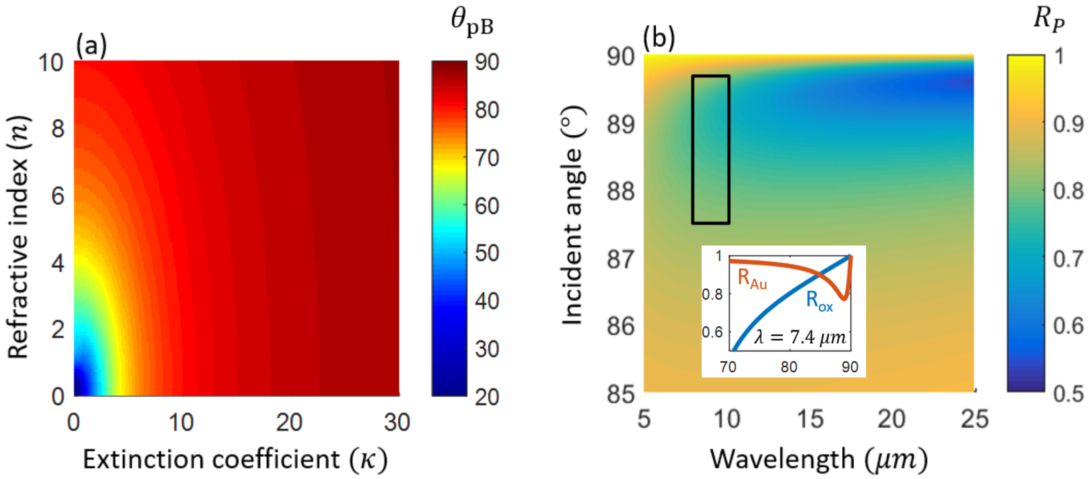

Figure 5-2) (a) Calculated pseudo-Brewster angle (θ_{pB}) for light incident from air onto a material with some arbitrary n and κ. (b) In the wavelength range in which the refractive index of SiO_2 is less than unity, the p-polarized reflectance of a gold mirror can decrease down to 75% because of the pseudo-Brewster effect.

Appendix C. Thermal emission measurements

When using an FTIR to measure thermal emission from a sample, one can generally describe the detected emission signal using the following equation [86], [106], [107] :

$$S_X(\lambda, T) = m(\lambda)[L_{BB}(\lambda, T)\varepsilon_x(\lambda, T) + B_X(\lambda, T)] \tag{S3-1}$$

where $S_X(\lambda, T)$ is measured spectrum, $m(\lambda)$ is the system response, $\varepsilon_x(\lambda, T)$ is the sample emissivity, $L_{BB}(\lambda, T)$ is the blackbody radiance, and $B_X(\lambda, T)$ is the background. Note here, we assume the most general case where sample emissivity can be dependent on temperature (such as our SNO sample investigated in chapter 4) and thus the background also depends on sample. We performed a systematic calibration of our FTIR using few known samples. Due to the balance between the background emission from the sample side and the detector side, the background signal turns out to be $-\varepsilon_x(\lambda, T)L_{BB}(\lambda, T_{room})$ and the system response for our FTIR is then:

$$S_X(\lambda, T) = \varepsilon_x(\lambda, T)m(\lambda)[L_{BB}(\lambda, T) - L_{BB}(\lambda, T_{room})] \tag{S3-2}$$

Using Eq. (S3-2), one can obtain the emissivity of an unknown sample from a known sample α via:

$$\varepsilon_x(\lambda, T) = \varepsilon_\alpha(\lambda, T)\ \frac{S_X(\lambda, T)}{S_\alpha(\lambda, T)} \tag{S3-3}$$

We utilized a lab blackbody (vertically aligned vertically aligned carbon nanotube (CNT) forest) as an was used to extract the emissivity of SNO sample at different temperatures. The emissivity of our blackbody is derived using direct emission measurements of silica and sapphire wafer, after the emissivity of these two samples are calibrated with the same number with reflection measurement. We assume this number is the black body emissivity $\varepsilon_{\alpha}(\lambda, T) = \varepsilon_{CNT} = 0.98$.

To confirm the accuracy of our direct emission measurement to measures the emissivity of our inverse opals on silicon absorber, we performed thermal emission measurements at normal incidence in two different ways using a Fourier transform spectrometer (Bruker Vertex 70 FTIR). The first way (used in the main text) had the sample in the sample compartment of the FTS, where we also mounted an angle-variable stage to enable the angle-dependent measurements described in the main text (Fig. 5-3 (a)). The emitted light was detected using a mercury cadmium telluride (MCT) detector in a Bruker Hyperion 2000 optical microscope connected to the output port on the right in Fig. 5-3 (a). The second method uses the same FTS, but with the sample at the situated in the microscope, and the beam traversing the opposite direction through the FTS, into a different MCT detector on the other side [Fig. 5-3 (b)]. We measured the normal-direction emissivity of the 4-μm-thick inverse opal sample on silicon and found the same results, performing the measurement in both directions [Fig. 5-3 (c)].

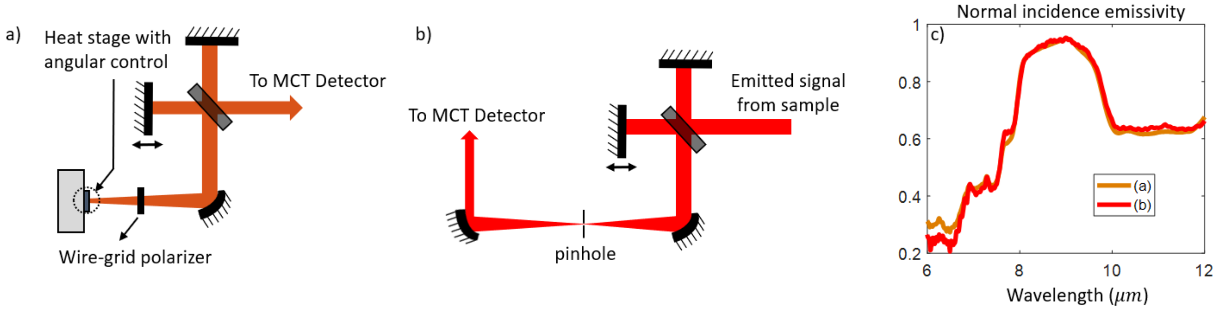

Figure 5-3) Diagrams that outline the two different paths for emission measurements in our Fourier-transform spectrometer (FTS) setup. (a) In this orientation, the emission signal comes from the custom-built angular stage holding the heater and the sample, while in (b) the emission signal comes from an infrared microscope

setup to a different MCT detector, after the light passes through the interferometer. (c) Measured emissivity for the two different paths of previous figure through direct emission measurement.

To confirm the accuracy of angular emission measurement, we compare results from direct emission measurements with angular reflectance measurements. Figures 5-4(a-b) show the ratio between the emissivity of silica and sapphire for three different incident angles (35, 45 and 55°) for both the s- and p-polarization, measured with two different techniques: direct emission (solid lines) and reflection (1-R, dashed lines) measurements. As seen in the plots, regardless of the method used to extract emissivity, in highly lossy spectral region for both silica and sapphire ($\lambda > 7\ \mu m$), the emissivities values are similar, validating our direct emission measurement at oblique incidence. Note that in the shorter wavelength spectral range that sapphire becomes semi-transparent, these ratios begin to vary because to calculate emissivity based on Kirchhoff's law we need to incorporate the transmission through sapphire wafer, which we do not do here.

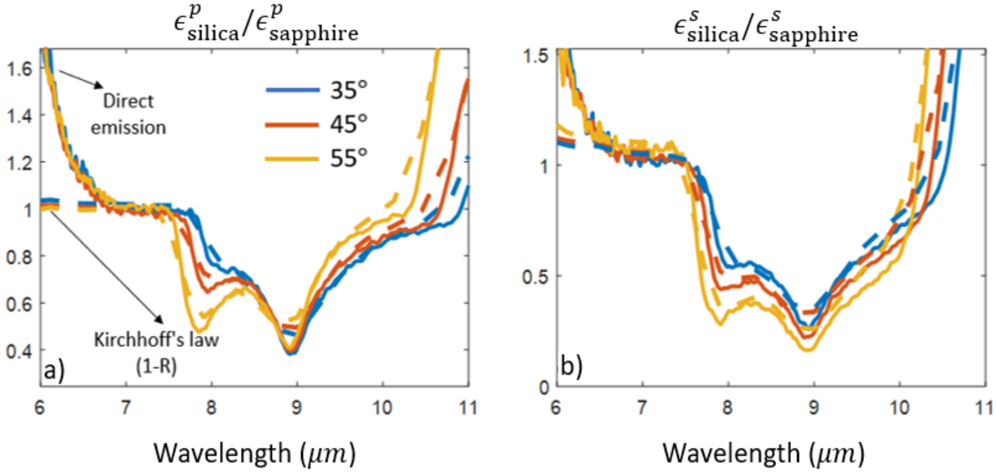

Figure 5-4) thermal emission verification data (a-b) Ratio of silica emissivity to sapphire emissivity at three different angles, resulted from direct emission measurement (solid lines) and oblique reflection measurement (dashed lines) and the application of Kirchhoff's law for (s) p-polarized, and (b) s-polarized light.

Appendix D. On the insulator-to-metal transition of samarium nickel oxide

As Figure 5-5 (a) shows, the resistance ~ temperature curve of SNO/Sapphire for both heating and cooling cycles are almost identical, demonstrating that there is no hysteresis in $SmNiO_3$. The electric resistance at room temperature increases by more than 4 fold compared with the metallic state due the thermally driven metal-insulator transitions. Figure 1 (b) shows the temperature derivate of resistance has a gradual sign change from negative to positive at ~ 140 °C because of the occurrence of the insulator-to-metal transition.

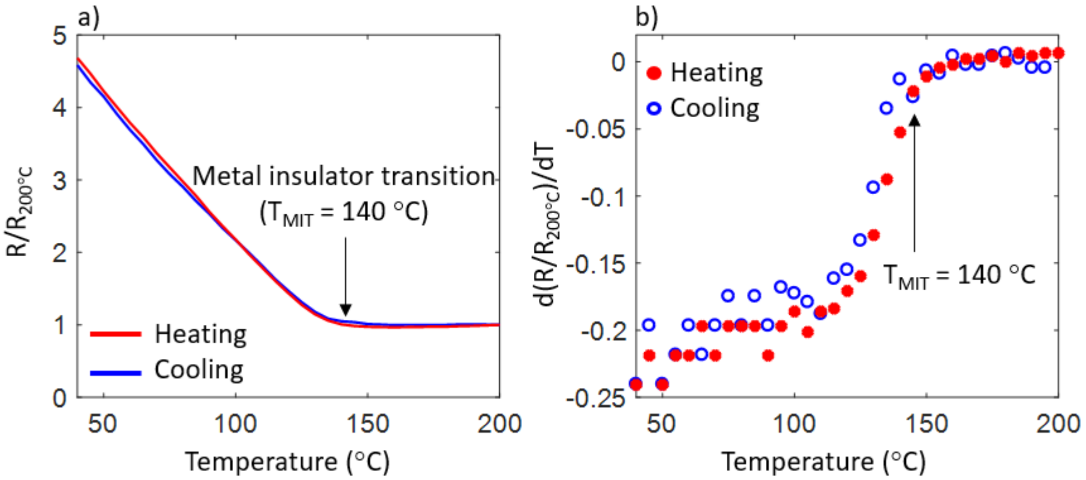

Figure 5-5) Metal insulator transition of SmNiO3 thin films grown on sapphire. (a) Normalized electrical resistance as a function of temperature for $SmNiO_3$ sample. The $SmNiO_3$ grown on sapphire substrate shows similar temperature dependent evolution of electrical resistance for both heating and cooling cycles. The metal insulator transition is ~ 140 °C [103](b) Temperature derivative of electrical resistance for $SmNiO_3$ on sapphire, which change sign from negative to position at ~ 140°C indicating the transition from insulating state to metallic state upon heating.

References

[1] E. D. Palik, *Handbook of optical constants of solids*, vol. 3. Academic Press, 1998.

[2] A. Sihvola, “Metamaterials in electromagnetics,” *Metamaterials*, vol. 1, no. 1, pp. 2–11, 2007.

[3] V. G. VESELAGO, “The Electrodynamics of Substances With Simultaneously Negative Values of ϵ and μ,” *Sov. Phys. uspekhi*, vol. 10, no. 4, pp. 509–514, 1968.

[4] J. B. Pendry, “Negative refraction makes a perfect lens,” *Phys. Rev. Lett.*, vol. 85, no. 18, pp. 3966–3969, 2000.

[5] R. A. Shelby, D. R. Smith, and S. Schultz, “Experimental Verification of a Negative Index of Refraction,” *Science (80-.).*, vol. 292, no. 5514, pp. 77–80, 2001.

[6] N. Engheta, “Tunneling of Electromagnetic Energy through Subwavelength Channels and Bends using " -Near-Zero Materials,” *Phys. Rev. Lett.*, vol. 157403, no. 15, pp. 1–4, 2006.

[7] I. Liberal and N. Engheta, “Near-zero refractive index photonics,” *Nat. Photonics*, vol. 11, no. 3, pp. 149–158, 2017.

[8] M. G. Silveirinha and N. Engheta, “Theory of supercoupling, squeezing wave energy, and field confinement in narrow channels and tight bends using ε near-zero metamaterials,” *Phys. Rev. B*, vol. 76, no. 24, p. 245109, 2007.

[9] U. Leonhardt, “Optical Conformal Mapping,” *Hunt Parathyroids*, vol. Science (80-.)., no. June, pp. 132–143, 2013.

[10] J. B. Khurgin, “How to deal with the loss in plasmonics and metamaterials,” *Nat.*

Nanotechnol., vol. 10, no. 1, pp. 2–6, 2015.

[11] G. P. Zhu AY, Kuznetsov AI, Luk’yanchuk B, Engheta N, “Traditional and emerging materials for optical metasurfaces,” *Nanophotonics*, vol. 6, no. 2, pp. 452–471, 2017.

[12] F. Y. Kischkat J, Peters S, Gruska B, Semtsiv M, Chashnikova M, Klinkmüller M, Fedosenko O, Machulik S, Aleksandrova A, Monastyrskyi G, “Mid-infrared optical properties of thin films of aluminum oxide , titanium dioxide , silicon dioxide , aluminum nitride , and silicon nitride,” *Appl. Opt.*, vol. 51, no. 28, pp. 6789–6798, 2012.

[13] J. D. Caldwell *et al.*, “Low-loss, infrared and terahertz nanophotonics using surface phonon polaritons,” *Nanophotonics*, vol. 4, no. 1, pp. 44–68, 2015.

[14] H. G. Tompkins, E. A. Irene, C. Hill, and N. Carolina, *Handbook of Ellipsometry*. 2005.

[15] S. J. Byrnes, “Multilayer optical calculations,” *arXiv*, no. 1603.02720, pp. 1–20, 2016.

[16] J. E. Olsen and F. Shimura, “Infrared reflection spectroscopy of the SiO2-silicon interface,” *J. Appl. Phys.*, vol. 66, no. 3, pp. 1353–1358, 1989.

[17] D. Attwood, *Soft X-rays and Extreme Ultraviolet*. 1999.

[18] B. T. Schwartz and R. Piestun, “Total external reflection from metamaterials with ultralow refractive index,” *JOSA B*, vol. 20, no. 12, pp. 2448–2453, 2003.

[19] Y. K. Mimura H, Yumoto H, Matsuyama S, Sano Y, Yamamura K, Mori Y, Yabashi M, Nishino Y, Tamasaku K, Ishikawa T, “Efficient focusing of hard x rays to by a total reflection mirror Efficient focusing of hard x rays to 25 nm by a total reflection mirror,” *Appl. Phys. Lett.*, vol. 90, no. 5, p. 051903, 2007.

[20] A. L. Ice GE, Chung JS, Tischler JZ, Lunt A, “Elliptical x-ray microprobe mirrors by

differential deposition Elliptical x-ray microprobe mirrors by differential deposition,” *Rev. Sci. Instrum.*, vol. 71, no. 7, pp. 2635–2639, 2000.

[21] B. T. Schwartz and R. Piestun, “Waveguiding in air by total external reflection from ultralow index metamaterials,” *Appl. Phys. Lett.*, vol. 85, no. 1, pp. 1–3, 2004.

[22] S. Babar and J. H. Weaver, “Optical constants of Cu , Ag , and Au revisited,” *Appl. Opt.*, vol. 54, no. 3, pp. 477–481, 2015.

[23] G. Y. B. Akimoto M, “Brewster and Pseudo-Brewster Angle Technique for Determination of Optical Constants,” *Jpn. J. Appl. Phys.*, vol. 1R, no. 31, p. 120, 1992.

[24] S. Y. Kim and K. Vedam, “Analytic solution of the pseudo-Brewster angle,” *JOSA A*, vol. 3, no. 11, pp. 1772–1773, 1986.

[25] E. Hecht, *Optics*. Pearson Education, 2016.

[26] R. L. Olmon *et al.*, “Optical dielectric function of gold,” *Phys. Rev. B - Condens. Matter Mater. Phys.*, vol. 86, no. 23, pp. 1–9, 2012.

[27] J. Y. Han, “Low-cost multi-touch sensing through frustrated total internal reflection,” *Proc. 18th Annu. Symp. user interface Softw. Technol. - UIST ’05.ACM*, pp. 115–118, 2005.

[28] R. R. Zhu S, Yu AW, Hawley D, “Frustrated total internal reflection,” *Am. J. Phys.*, vol. 54, no. 7, pp. 601–607, 1986.

[29] A. R. Hind and A. M. Bhargava, Suresh K, “At the solid/liquid interface: FTIR/ATR--the tool of choice,” *Adv. Colloid Interface Sci.*, vol. 93, no. 1–3, pp. 91–114, 2001.

[30] E. M. Lucarini, V., Saarinen, J. J., Peiponen, K. E., & Vartiainen, *Kramers-Kronig*

relations in optical materials research. Springer Science & Business Media, 2005.

[31] J. Kim, G. V Naik, N. K. Emani, U. Guler, and A. Boltasseva, “Plasmonic Resonances in Nanostructured Transparent Conducting Oxide Films,” *IEEE J. Sel. Top. Quantum Electron.*, vol. 19, no. 3, pp. 4601907–4601907, 2013.

[32] D. W. Spitzer, W. G., Kleinman, D., “Infrared Properties of Hexagonal Silicon Carbide,” *Phys. Rev.*, vol. 113, no. 1, p. 127, 1959.

[33] J. R. Jasperse, A. Kahan, J. N. Plendl, and S. S. Mitra, “Temperature dependence of infrared dispersion in ionic crystals LiF and MgO,” *Phys. Rev.*, vol. 146, no. 2, pp. 526–542, 1966.

[34] L. E. Kaiser, W., Spitzer, W. G., Kaiser, R. H., & Howarth, “Infrared Properties of CaF2, SrF2, and BaF2,” *Phys. Rev.*, vol. 127, no. 1956, pp. 1950–1954, 1962.

[35] E. Kretschmann, “Die Bestimmung optischer Konstanten von Metallen durch Anregung von Oberfliichenplasmaschwingungen,” *Zeitschrift für Phys. A Hadron. Nucl.*, vol. 241, no. 4, pp. 313–324, 1971.

[36] A. Otto, “Excitation of nonradiative surface plasma waves in silver by the method of frustrated total reflection,” *Zeitschrift für Phys. A Hadron. Nucl.*, vol. 410, pp. 398–410, 1968.

[37] W. L. Barnes, A. Dereux, and T. W. Ebbesen, “Surface plasmon subwavelength optics,” *Nature*, vol. 424, no. 6950, pp. 824–830, 2003.

[38] D. W. Berreman, “Infrared Absorption at Longitudinal Optic Frequency in Cubic Crystal Films,” *Phys. Rev.*, vol. 130, no. 6, p. 2193, 1963.

[39] S. Campione, I. Brener, and F. Marquier, “Theory of epsilon-near-zero modes in ultrathin films,” vol. 121408, pp. 1–5, 2015.

[40] Y. Yang *et al.*, “Femtosecond optical polarization switching using a cadmium oxide-based perfect absorber,” *Nat. Photonics*, vol. 11, no. 6, pp. 390–395, 2017.

[41] A. Shahsafi *et al.*, “Mid-infrared Optics Using Dielectrics with Refractive Indices below Unity,” *Phys. Rev. Appl.*, vol. 10, no. 3, p. 1, 2018.

[42] J. Kischkat *et al.*, “Mid-infrared optical properties of thin films of aluminum oxide, titanium dioxide, silicon dioxide, aluminum nitride, and silicon nitride,” *Appl. Opt.*, vol. 51, no. 28, pp. 6789–6798, 2012.

[43] G. A. Niklasson and C. G. Granqvist, “Effective medium models for the optical properties of inhomogeneous materials,” *Appl. Opt.*, vol. 20, no. 1, p. 26, 1981.

[44] W. Lee and S. Park, “Porous Anodic Aluminum Oxide : Anodization and Templated Synthesis of Functional Nanostructures,” 2014.

[45] I. Yamada, K. Takano, M. Hangyo, M. Saito, and W. Watanabe, “Terahertz wire-grid polarizers with micrometer-pitch Al gratings,” vol. 34, no. 3, pp. 274–276, 2009.

[46] S. H. Kim, J. Park, and K. Lee, “Fabrication of a nano-wire grid polarizer for brightness enhancement in liquid crystal display,” 2006.

[47] Masataka Shirasaki, “Prism Polarizer,” 1983.

[48] J. Schwarzmuller, “Multilayer brewster angle polarization device,” 1975.

[49] D. J. Dummer, S. G. Kaplan, L. M. Hanssen, and A. S. Pine, “High-quality Brewsters’ angle polarizer for broadband infrared application.”

[50] A. You, M. A. Y. Be, and I. In, “Gigahertz tunable waveguide CO 2 laser,” vol. 304, no. October, pp. 23–26, 2003.

[51] R. Boyd, “Radiometry and the detection of optical radiation,” 1983.

[52] J. Mink, *Handbook of Vibrational Spectroscopy*. New York, NY: Wiley, 2006.

[53] H. Kaplan, *Practical Applications of Infrared Thermal Sensing and Imaging Equipment*, 3rd ed. Bellingham: SPIE, 2007.

[54] M. Vollmer and K.-P. Möllmann, *Infrared Thermal Imaging*. Weinheim, Germany: Wiley-VCH Verlag GmbH & Co. KGaA, 2017.

[55] Y. Xie, X. Fan, J. D. Wilson, R. N. Simons, Y. Chen, and J. Q. Xiao, “A universal electromagnetic energy conversion adapter based on a metamaterial absorber,” *Sci. Rep.*, vol. 4, p. 6301, 2014.

[56] M. L. Wu, S. H., Chen, M., Barako, M. T., Jankovic, V., Hon, P. W., Sweatlock, L. A., & Povinelli, “Thermal homeostasis using microstructured phase-change materials,” *optica*, vol. 4, no. 11, p. 1390, 2017.

[57] S. Azoubel, R. Cohen, and S. Magdassi, “Wet deposition of carbon nanotube black coatings for stray light reduction in optical systems,” *Surf. Coatings Technol.*, vol. 262, pp. 21–25, 2015.

[58] A. Buffington, B. V Jackson, and C. M. Korendyke, “Wide-angle stray-light reduction for a spaceborne optical hemispherical imager,” *Appl. Opt.*, vol. 35, no. 34, pp. 6669–6673, 1996.

[59] N. Liu, M. Mesch, T. Weiss, M. Hentschel, and H. Giessen, “Infrared perfect absorber and

its application as plasmonic sensor," *Nano Lett.*, vol. 10, no. 7, pp. 2342–2348, 2010.

[60] F. Cheng, X. Yang, and J. Gao, "Enhancing intensity and refractive index sensing capability with infrared plasmonic perfect absorbers," *Opt. Lett.*, vol. 39, no. 11, pp. 3185–3188, 2014.

[61] G. Li, X. Chen, O. Li, and C. Shao, "A novel plasmonic resonance sensor based on an infrared perfect absorber," *J. Phys. D. Appl. Phys.*, vol. 45, no. 20, p. 205102, 2012.

[62] C. Wu, Y. Avitzour, and G. Shvets, "Ultra-thin wide-angle perfect absorber for infrared frequencies," *Metamaterials Fundam. Appl.*, vol. 7029, no. 2008, p. 70290W, 2008.

[63] M. Diem, T. Koschny, and C. M. Soukoulis, "Wide-angle perfect absorber/thermal emitter in the terahertz regime," *Phys. Rev. B - Condens. Matter Mater. Phys.*, vol. 79, no. 3, pp. 1–4, 2009.

[64] X. Liu, T. Tyler, T. Starr, A. F. Starr, N. M. Jokerst, and W. J. Padilla, "Taming the blackbody with infrared metamaterials as selective thermal emitters," *Phys. Rev. Lett.*, vol. 107, no. 4, pp. 4–7, 2011.

[65] D. G. Baranov, Y. Xiao, I. A. Nechepurenko, A. Krasnok, and A. Alù, "Nanophotonic engineering of far-field thermal emitters," *Nat. Mater.*, vol. 1, 2019.

[66] C. M. Watts, X. Liu, and W. J. Padilla, "Metamaterial electromagnetic wave absorbers," *Adv. Mater.*, vol. 24, no. 23, 2012.

[67] J. Hao, J. Wang, X. Liu, W. J. Padilla, L. Zhou, and M. Qiu, "High performance optical absorber based on a plasmonic metamaterial," *Appl. Phys. Lett.*, vol. 96, no. 25, pp. 10–13, 2010.

[68] C. Wu *et al.*, “Large-area wide-angle spectrally selective plasmonic absorber,” *Phys. Rev. B - Condens. Matter Mater. Phys.*, vol. 84, no. 7, pp. 1–7, 2011.

[69] M. Zhou, H. Song, X. Xu, A. Shahsafi, Z. Xia, and Z. Ma, “Accelerating vapor condensation with daytime radiative cooling,” *arXiv*, no. 1804.10736, 2018.

[70] S. F. Wei Li, “Nanophotonic control of thermal radiation for energy applications [Invited],” *Opt. Express*, vol. 26, no. 12, pp. 15101–15109, 2018.

[71] K. Mizuno *et al.*, “A black body absorber from vertically aligned single-walled carbon nanotubes,” *Proc. Natl. Acad. Sci.*, vol. 106, no. 15, pp. 6044–6047, 2009.

[72] J. long Kou, Z. Jurado, Z. Chen, S. Fan, and A. J. Minnich, “Daytime Radiative Cooling Using Near-Black Infrared Emitters,” *ACS Photonics*, vol. 4, no. 3, pp. 626–630, 2017.

[73] B. Hatton, L. Mishchenko, S. Davis, K. H. Sandhage, and J. Aizenberg, “Assembly of large-area, highly ordered, crack-free inverse opal films,” *Proc. Natl. Acad. Sci.*, vol. 107, no. 23, pp. 10354–10359, 2010.

[74] E. Shirman *et al.*, “Modular Design of Advanced Catalytic Materials Using Hybrid Organic – Inorganic Raspberry Particles,” *Adv. Funct. Mater.*, vol. 1704559, no. 27, pp. 1–20, 2018.

[75] N. V. and J. A. Katherine R. Phillips, Grant T. England, Steffi Sunny, Elijah Shirman, Tanya Shirman, “A colloidoscope of colloid-based porous materials and their uses,” *Chem. Soc. Rev.*, vol. 45, no. 2, 2016.

[76] I. B. Burgess, N. Koay, K. P. Raymond, M. Kolle, M. Lon, and B. E. T. Al, “Wetting in Color : Colorimetric Differentiation of Organic Liquids with High Selectivity,” *ACS Nano*, vol. 6, no. 2, pp. 1427–1437, 2012.

[77] K. R. Phillips, N. Vogel, I. B. Burgess, C. C. Perry, and J. Aizenberg, "Directional Wetting in Anisotropic Inverse Opals," *Langmuir*, vol. 30, no. 25, p. 7615, 2014.

[78] I. B. Burgess, L. Mishchenko, B. D. Hatton, M. Kolle, M. Lon, and J. Aizenberg, "Encoding Complex Wettability Patterns in Chemically Functionalized," *J. Am. Chem. Soc.*, vol. 133, no. 32, pp. 12430–12432, 2011.

[79] P. Munnik, P. E. De Jongh, and K. P. De Jong, "Recent Developments in the Synthesis of Supported Catalysts," *Chem. Rev.*, vol. 115, no. 14, p. 6687, 2015.

[80] Y. Nishijima *et al.*, "Inverse silica opal photonic crystals for optical sensing applications," *Opt. Express*, vol. 15, no. 20, p. 12979, 2007.

[81] V. S. Wenshan Cai, *Optical Metamaterials: Fundamentals and Applications*. Springer, 2010.

[82] H. A. Macleod, *Thin-Film Optical Filters University of Arizona*. 1969.

[83] S. Chen *et al.*, "Polarization insensitive and omnidirectional broadband near perfect planar metamaterial absorber in the near infrared regime," *Appl. Phys. Lett.*, vol. 99, no. 25, pp. 2009–2012, 2011.

[84] P. Bouchon, C. Koechlin, F. Pardo, R. Haïdar, and J. Pelouard, "Wideband omnidirectional infrared absorber with a patchwork of plasmonic nanoantennas," *Opt. Lett.*, vol. 37, no. 6, pp. 1038–1040, 2012.

[85] J. T. et. al. Roney, P., Shahsafi, A., Zhou, Y., Zhang, Z., Xiao, Y., Wan, C., Wambold, R., Salman, J., Yu, Z., Li, J., Sadowski, "Temperature-independent thermal radiation," *arXiv*, no. 1902.00252, 2019.

[86] Y. Xiao *et al.*, “Measuring Thermal Emission Near Room Temperature Using Fourier-Transform Infrared Spectroscopy,” *Phys. Rev. Appl.*, vol. 10, no. 1, p. 1, 2019.

[87] R. H. Goodwin, J. W., Hearn, J., Ho, C. C., & Ottewill, “Studies on the preparation and characterisation of monodisperse polystyrene latices,” *colloid Polym. Sci.*, vol. 471, pp. 464–471, 1974.

[88] M. Benkahoul *et al.*, “Thermochromic VO2 film deposited on Al with tunable thermal emissivity for space applications,” *Sol. Energy Mater. Sol. Cells*, vol. 95, no. 12, pp. 3504–3508, Dec. 2011.

[89] S.-H. Wu *et al.*, “Thermal homeostasis using microstructured phase-change materials,” *Optica*, vol. 4, no. 11, p. 1390, Nov. 2017.

[90] M. A. Kats *et al.*, “Vanadium Dioxide as a Natural Disordered Metamaterial: Perfect Thermal Emission and Large Broadband Negative Differential Thermal Emittance,” *Phys. Rev. X*, vol. 3, no. 4, p. 041004, 2013.

[91] D. M. Bierman *et al.*, “Radiative Thermal Runaway Due to Negative-Differential Thermal Emission Across a Solid-Solid Phase Transition,” *Phys. Rev. Appl.*, vol. 10, no. 2, p. 021001, 2018.

[92] K. Joulain, Y. Ezzahri, J. Drevillon, and P. Ben-Abdallah, “Modulation and amplification of radiative far field heat transfer: Towards a simple radiative thermal transistor,” *Appl. Phys. Lett.*, vol. 106, no. 13, p. 133505, Mar. 2015.

[93] S. D. Ha, M. Otaki, R. Jaramillo, A. Podpirka, and S. Ramanathan, “Stable metal–insulator transition in epitaxial SmNiO3 thin films,” *J. Solid State Chem.*, vol. 190, pp. 233–237, Jun. 2012.

[94] S. Catalano *et al.*, “Electronic transitions in strained SmNiO $_3$ thin films,” *APL Mater.*, vol. 2, no. 11, p. 116110, Nov. 2014.

[95] J. Pérez-Cacho, J. Blasco, J. García, M. Castro, and J. Stankiewicz, “Study of the phase transitions in SmNiO3,” *J. Phys. Condens. Matter*, vol. 11, no. 2, pp. 405–415, Jan. 1999.

[96] S. Catalano, M. Gibert, J. Fowlie, J. Íñiguez, J.-M. Triscone, and J. Kreisel, “Rare-earth nickelates *R* NiO $_3$: thin films and heterostructures,” *Reports Prog. Phys.*, vol. 81, no. 4, p. 046501, Apr. 2018.

[97] V. A. Klimov, I. O. Timofeeva, S. D. Khanin, E. B. Shadrin, A. V. Ilinskii, and F. Silva-Andrade, “Hysteresis loop construction for the metal-semiconductor phase transition in vanadium dioxide films,” *Tech. Phys.*, vol. 47, no. 9, pp. 1134–1139, Sep. 2002.

[98] G. Catalan, “Progress in perovskite nickelate research,” *Phase Transitions*, vol. 81, no. 7–8, pp. 729–749, Jul. 2008.

[99] J. Ruppen *et al.*, “Impact of antiferromagnetism on the optical properties of rare-earth nickelates,” *Phys. Rev. B*, vol. 96, no. 4, p. 045120, Jul. 2017.

[100] M. A. Kats and F. Capasso, “Optical absorbers based on strong interference in ultra-thin films,” *Laser Photon. Rev.*, vol. 10, no. 5, pp. 735–749, Jun. 2016.

[101] M. Schubert, T. E. Tiwald, and C. M. Herzinger, “Infrared dielectric anisotropy and phonon modes of sapphire,” *Phys. Rev. B*, vol. 61, no. 12, pp. 8187–8201, Mar. 2000.

[102] Y. Xiao *et al.*, “Thermal-emission measurements near room temperature using Fourier-transform infrared spectroscopy,” Jul. 2018.

[103] A. Shahsafi *et al.*, “Temperature-independent thermal radiation,” *Proc. Natl. Acad. Sci.*,

vol. 116, no. 52, p. 26402, 2019.

[104] J. W. Salisbury and D. M. D’Aria, “Emissivity of terrestrial materials in the 8–14 µm atmospheric window,” *Remote Sens. Environ.*, vol. 42, no. 2, pp. 83–106, Nov. 1992.

[105] H. G. Tompkins, E. A. Irene, C. Hill, and N. Carolina, *Handbook of Ellipsometry*. 2005.

[106] Y. Xiao *et al.*, “Precision Measurements of Temperature-Dependent and Nonequilibrium Thermal Emitters,” *Laser Photon. Rev.*, vol. 14, no. 8, pp. 1–17, 2020.

[107] C. Yao *et al.*, “Correcting thermal-emission-induced detector saturation in infrared spectroscopy,” *arXiv*, vol. 2012.14987, pp. 1–15, 2020.